A petrological, mineralogical, and chemical analysis of the lunar mare basalt meteorite LaPaz Icefield 02205, 02224, and 02226

Katherine H. JOY[1, 2, 3*], Ian A. CRAWFORD[1], Hilary DOWNES[1],
Sara S. RUSSELL[2], and Anton T. KEARSLEY[2]

[1]UCL/Birkbeck Research School of Earth Sciences, University College London, Gower Street, London, WC1E 6BT, UK
[2]The Natural History Museum London, Cromwell Road, London, SW7 5BD, UK
[3]The Rutherford Appleton Laboratory, Chilton, Didcot, OX11 0QX, UK
[*]Corresponding author. E-mail: k.joy@ucl.ac.uk

Abstract–LaPaz Icefield (LAP) 02205, 02226, and 02224 are paired stones of a crystalline basaltic lunar meteorite with a low-Ti (3.21–3.43% TiO_2) low-Al (9.93–10.45% Al_2O_3), and low-K (0.11–0.12% K_2O) composition. They consist mainly of zoned pyroxene and plagioclase grains, with minor ilmenite, spinel, and mesostasis regions. Large, possibly xenocrystic, forsteritic olivine grains (<3% by mode) contain small trapped multiphase melt inclusions. Accessory mineral and mesostasis composition shows that the samples have experienced residual melt crystallization with silica oversaturation and late-stage liquid immiscibility. Our section of LAP 02224 has a vesicular fusion crust, implying that it was at one time located sufficiently close to the lunar surface environment to have accumulated solar-wind-implanted gases.

The stones have a comparable major element composition and petrography to low-Ti, low-Al basalts collected at the Apollos 12 and 15 landing sites. However, the LAP stones also have an enriched REE bulk composition and are more ferran (Mg numbers in the range of 31 to 35) than similar Apollo samples, suggesting that they represent members of a previously unsampled fractionated mare basalt suite that crystallized from a relatively evolved lunar melt.

INTRODUCTION

Manned and unmanned missions to the Moon have returned about 382 kg of lunar rocks and soils (Vaniman et al. 1991). These were all collected from rather atypical regions on the lunar near side, within and around the Procellarum KREEP Terrane (PKT) (Jolliff et al. 2000), or from equatorial latitudes on the eastern limb. Interpretations of the nature of the lunar crust and mantle have therefore been made from a data set from geographically restricted areas of the Moon. In contrast, lunar meteorites are derived from random sample sites on the surface, and thus provide a wealth of new information about the nature of the Moon, even though their precise provenance is as of yet unknown.

LAP 02205, 02224, 02226, 02436, and 03632 (Fig. 1) are paired stones of a single meteorite body. They were collected from the LaPaz Icefield in central western Antarctica by the Antarctic Search for Meteorites program (ANSMET) from 2002 to 2004 (Satterwhite 2003, 2004a, 2004b). They have been classified as lunar material based on several lines of evidence. Their mineralogy is typical of a highly reducing and dry environment typically associated with lunar magmatic conditions, and their oxygen isotope ratios ($\delta^{18}O$ = +5.6‰ and $\delta^{17}O$ = 2.7‰) (Satterwhite 2003) fall near the terrestrial-lunar fractionation line (TLFL). Our own analysis of bulk rock element ratios (Table 1) of Ba/Rb (63–78), K/U (1496–1570), and FeO/MnO (77–78) are also typical of lunar rocks (BVSP 1981; Warren 2005), and the Fe/Mn ratios in pyroxenes and olivines (Fig. 2) plot close to the lunar fractionation trend (Dymek et al. 1976; Papike 1998; Anand et al. 2003a; Papike et al. 2003; Cahill et al. 2004). With a combined mass of ~1.8 kg, they represent the largest mass of lunar meteoritic material yet found in Antarctica.

In this paper, we present the petrography of LAP 02205, LAP 02224, and LAP 02226 and the bulk compositions of LAP 02205 and LAP 02224. Using mineralogical (Table 5) and bulk chemical comparisons (Table 1), we discuss pairing relationships among the stones and infer the nature of the lunar launch site. We shall discuss the samples' magmatic history and place them in the context of the lunar rock collection. Based on our measured bulk composition analysis (Table 1) and following the classification scheme of Neal and
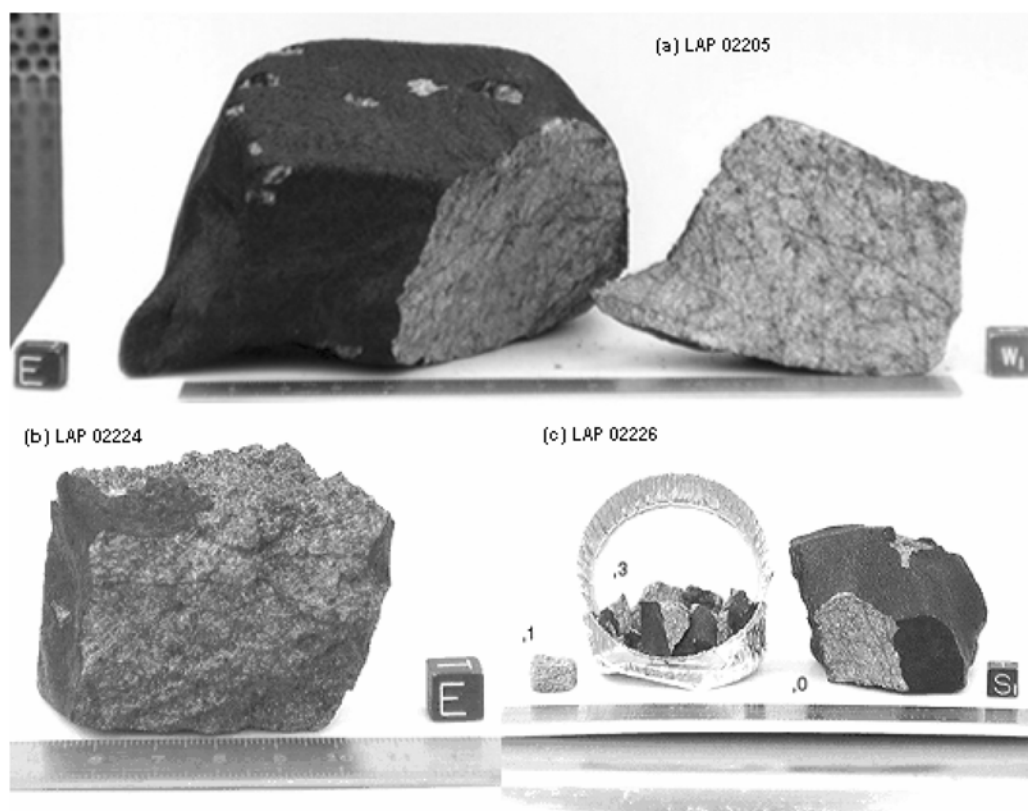
Fig. 1. Photographs of a) LAP 02205, b) LAP 02224, and c) LAP 02226 stones in hand specimen. All three stones have a dark brown/black fusion crust. The scale cube is 1 cm on a side. Photographs courtesy of Satterwhite (2003, 2004a).

Taylor (1992), we classify LAP 02205, 02204, and 02226 as low-Ti (3.21–3.43% TiO_2), low-Al (9.93–10.45% Al_2O_3), and low-K (0.11–0.12% K_2O) crystalline basalts. This low-Ti classification is also consistent with the recent results of Righter et al. (2005), Zeigler (2005), Day et al. (2006), and Anand et al. (2006), who have also discussed the LAP stones.

ANALYTICAL METHODS

The Meteorite Working Group kindly provided polished thin sections of LAP 02205,32 (with an area of ~10 × 12 mm), LAP 02224,35 (~5.5 × 14.1 mm), and LAP 02226,25 (~5.8 × 8.4 mm). We determined the major and minor element concentrations in the constituent phases of these sections using a Cameca SX-50A wavelength dispersive electron microprobe (EMP) at the Natural History Museum London (NHM). The Cameca was operated at a 20 keV accelerating voltage with a 20 nA beam current with a focused beam analysis for 10–30 s count time per element, and employed well-characterized silicate, oxide, and metal standards. In spinel investigations, results were corrected for an instrumental V, Ti peak overlap; in FeNi investigations, results were corrected for the Fe, Co overlap. X-ray maps and additional mineral composition data were determined by electron dispersive spectrometry using a JEOL 5900LV SEM

and a LEO 1455VP SEM at the NHM, both fitted with an Oxford Instruments INCA energy dispersive X-ray microanalyzer system and operated at a 20 kV accelerating voltage and 2 nA beam current. Both instruments were calibrated with well-characterized samples. X-ray maps were taken at a resolution of 256 × 256 pixels and at a magnification of 200–250 for large whole sample maps, and at higher magnification (200–900) for individual area studies.

We measured the concentration of trace elements in mineral phases by time-resolved analysis using a laser ablation inductively coupled plasma mass spectrometer (LA-ICP-MS) at the NHM. The instrument was a VG Plasma Quad, coupled to a 213 nm laser. Carrier gases were a mix of Ar and He. Analyses were performed in situ, with a 80 × 150 µm raster, forming an elongated ablated pit. The ablated volume allowed compositional information to be obtained for individual mineral phases and mesostasis regions. Measurements were made for 120 s, during which time the abundance of 36 elements was monitored. Background conditions were monitored for 60 s and the laser ablated the sample for 60 s. The external standard used was NIST 612 (a synthetic doped glass). The standard deviations of the NIST 612 measurements were between 2 and 10% for the elements analyzed. Calcium was used as an internal standard by comparing the CaO abundance in minerals also measured by the EMP. We ensured that the laser was directed to the

Table 1. Bulk major (oxide wt%), minor and trace element (ppm) composition analyses of LAP 02205 and LAP 02224, obtained using ICP-AES ([a]) and ICP-MS ([b]) compared to bulk rock analysis by other authors. The quoted errors are the standard deviations for 5 (major element) and 3 (minor and trace element) independent analyses of each sample. A dash (–) means not reported. The reported material mass is the total used for the complete bulk analysis and is given in milligrams (mg).

|	LAP 02224,31	LAP 02205,13	Anand et al. 2006 LAP 02205	Zeigler et al. 2005 LAP average	Day et al. 2006 LAP 02205	Day et al. 2006 LAP 02224
SiO_2[a]	44.57 ± 0.20	44.53 ± 0.14	45.2	45.3	46	45.3
TiO_2[a]	3.21 ± 0.02	3.43 ± 0.13	3.38	3.11	3.11	3.27
Al_2O_3[a]	9.93 ± 0.05	10.13 ± 0.03	10	9.79	9.95	9.95
Cr_2O_3[a]	0.29 ± 0.01	0.34 ± 0.01	0.19	0.31	0.29	0.3
FeO[a]	21.29 ± 0.17	21.69 ± 0.18	23.2	22.2	21.8	22
MnO[a]	0.28 ± 0.01	0.28 ± 0.01	0.23	0.29	0.32	0.29
MgO[a]	6.47 ± 0.03	5.58 ± 0.02	5.99	6.63	6.32	6.84
CaO[a]	10.99 ± 0.07	11.23 ± 0.11	11.2	11.09	11.4	11.3
Na_2O[a]	0.41 ± 0.01	0.42 ± 0.01	0.33	0.38	0.39	0.38
K_2O[a]	0.11 ± 0.01	0.12 ± 0.01	0.11	0.07	0.1	0.11
P_2O_5[a]	0.11 ± 0.01	0.12 ± 0.01	0.12	0.1	0.17	0.16
Total	97.36	97.53	100	99.28	99.85	99.9
Mg #	35.16	31.45	31.4	34.7	34.1	35.7
Li[a]	14 ± 0.04	13 ± 0.11	11.7	–	–	–
Be[b]	1.18 ± 0.07	1.1 ± 0.09	1.37	–	–	–
Sc[a]	61 ± 0.04	59 ± 0.32	58.6	59.2	52.80	57.3
V[a]	118 ± 0.33	107 ± 0.11	129	–	92	109
Co[a]	38 ± 0.26	35 ± 0.26	37.3	37	35.4	36.9
Ni[a]	35 ± 0.44	17 ± 0.11	27.6	–	42.4	18.5
Cu[a]	12 ± 0.06	12 ± 0.12	–	–	18.6	19.4
Zn[a]	16 ± 0.26	13 ± 0.34	–	–	27.5	29.6
Ga[b]	6.68 ± 0.19	5.24 ± 0.18	–	–	3.74	4.07
Rb[b]	2.15 ± 0.11	2.18 ± 0.07	2.1	–	1.67	1.74
Sr[a]	143 ± 1.17	135 ± 1.57	135.3	133	109	122
Y[a]	68 ± 0.11	80 ± 0.10	73.2	–	57	64.9
Zr[b]	198 ± 2.12	185 ± 2.18	200.3	183	172	190
Nb[b]	13.6 ± 0.09	13.2 ± 0.17	14.7	–	11.90	12.9
Cs[b]	0.22 ± 0.01	0.07 ± 0.01	0.1	–	0.03	0.04
Ba[b]	136 ± 0.54	170 ± 0.41	137	145	122	131
La[b]	13 ± 0.34	14.3 ± 0.34	13.4	13.1	9.97	11.5
Ce[b]	33 ± 0.77	36.2 ± 0.94	37.31	34.7	26.3	29.3
Pr[b]	4.92 ± 0.15	5.35 ± 0.11	5.15	–	4.04	4.5
Nd[b]	24.1 ± 0.66	26.5 ± 0.86	25.12	22	19.1	21.5
Sm[b]	7.91 ± 0.23	8.4 ± 0.15	7.56	7.74	6.05	6.73
Eu[b]	1.45 ± 0.04	1.49 ± 0.04	1.24	1.24	0.98	1.07
Gd[b]	9.54 ± 0.34	10.8 ± 0.34	9.95	–	7.81	8.73
Tb[b]	1.89 ± 0.06	2.1 ± 0.05	1.93	1.79	1.44	1.62
Dy[b]	12.1 ± 0.40	13.6 ± 0.41	12.08	–	9.35	10.4
Ho[b]	2.64 ± 0.09	2.91 ± 0.09	2.45	–	2.00	2.21
Er[b]	7.39 ± 0.23	8.35 ± 0.25	6.71	–	5.40	6.04
Tm[b]	1.06 ± 0.03	1.17 ± 0.03	0.94	–	0.84	0.94
Yb[b]	6.72 ± 0.19	7.61 ± 0.21	6.37	6.59	5.30	5.91
Lu[b]	0.95 ± 0.04	1.07 ± 0.04	0.88	0.92	0.82	0.9
Hf[b]	4.8 ± 0.13	5.74 ± 0.13	5.39	5.58	4.50	4.92
Ta[b]	0.75 ± 0.03	0.86 ± 0.03	0.77	0.71	0.60	0.65
W[b]	0.92 ± 0.11	0.57 ± 0.08	0.2	–	–	–
Pb[b]	1.29 ± 0.02	1.45 ± 0.01	1	–	0.71	0.80
U[b]	0.58 ± 0.01	0.67 ± 0.01	0.55	0.52	0.45	0.50
Th[b]	2.17 ± 0.03	2.5 ± 0.07	2.33	2.04	1.79	2.04
Mass (mg)	140	140	100	641 (27–48 mg per sample)	~30	~30
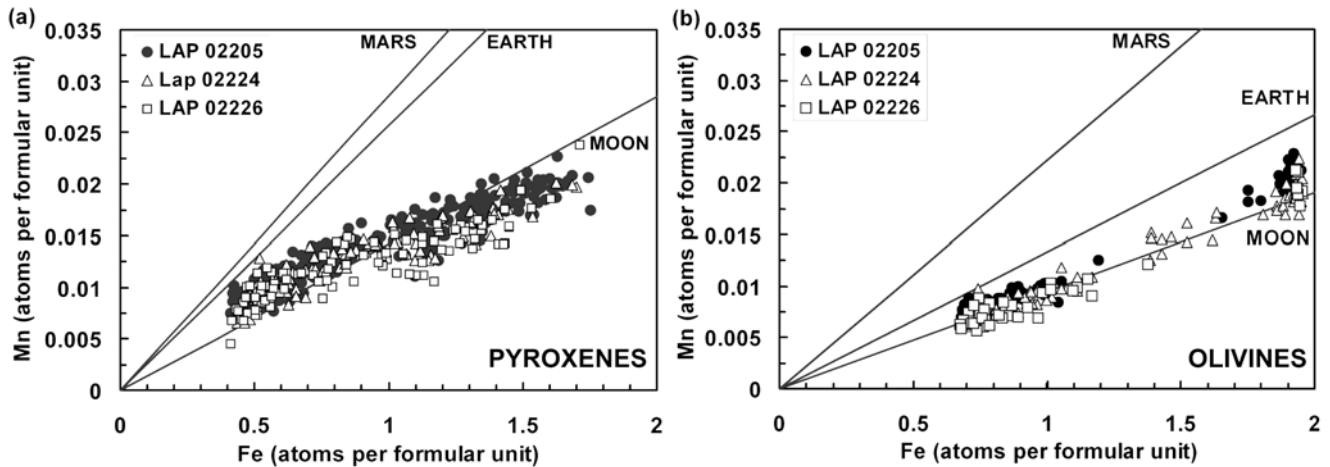
Fig. 2. Fe to Mn ratios in pyroxenes and olivines are an indicator of planetary origin as lunar pyroxenes and olivines exhibit diagnostic Fe/Mn ratios compared to the Earth, Mars, Vesta, and chondrites, probably as the result of volatile loss in an early Moon-forming event (Papike et al. 2003). Fe-Mn ratios in LAP 02205, 02224, and 02226 (Tables 2 and 3) for a) pyroxenes and b) olivines compared to typical planetary fractionation trends complied by Papike et al. (2003). Atoms per formula unit are based on 4 oxygen atoms for olivine and 6 oxygens for pyroxene.

center of the mineral grain/mesostasis area to avoid contamination from surrounding crystals. There is a risk that in three dimensions the laser beam can penetrate to the glass slide, however, the raster process reduces this risk and the glass slide has distinctive HREE patterns that ensure that any sampling errors can be removed in the calibration process.

We determined the whole-rock major, minor, and trace element composition of chippings of LAP 02205,13 (original mass: 209 mg) and LAP 02224,31 (original mass: 216 mg) by inductively coupled plasma-atomic emission spectrometry (ICP-AES) and mass spectrometry (ICP-MS) at the NHM. The instruments used were a Varian VISTA PRO Axial ICP-AES and a Varian ICP-MS. We ground the chips using an agate mortar and pestle in a clean room environment to minimize external contamination. For the major elements, 40 mg of powdered material was fused with $LiBO_2$ flux and then dissolved in dilute HNO_3. For the trace elements, an HF/$HClO_4$/HNO_3 dissolution was undertaken using 100 mg of sample. Both dissolution methods were based on those of Thompson and Walsh (2003). Five analyses were completed for each sample to determine measurement precision; the average bulk element concentration is given in Table 1. Major elements were determined by ICP-AES; the instrument was calibrated with NHM certified reference materials (CRMs; Mica-Fe, NIM-D, NIM-N, NIM-P). Selected trace elements were also determined by ICP-AES after calibration using the standard NHM synthetic standards, and matrix corrected with CRMs (W1, BHVO-1, BCR-1). Remaining trace elements were determined by ICP-MS, again calibrated with synthetic standards, using Rh and In as internal standards, and with CRMs (BCR-1, BHVO-1) used to check the data quality. Some minor and trace elements were measured by both techniques and are generally in good agreement (Table 1).

We calculated modal mineralogy using the Oxford

Instruments INCA Phasemap tool (Table 5). This software allows us to identify mineralogical phases using ternary element plots of specific pixel information from montaged X-ray maps of the samples (Fig. 3). The major source of uncertainty in this determination of mineral modes is due to difficulties in determining exact phase boundaries, but by combining several of these plots, representative mineral proportions can be estimated (Fig. 3d).

RESULTS

Petrography

LAP 02205, 02224, and 02226 are unbrecciated holocrystalline basalts. The stones are often cut by fractures and minor black, glassy melt veins (Fig. 1). They are coarse-grained, with pyroxenes and forsteritic olivine phases sometimes being >1 mm, and typically exceeding 500 μm in length. There are some minor differences between the three studied sections. LAP 02205,32, the largest of the three thin sections, contains parallel minor fault structures with associated opaque black melt. LAP 02224,35 is slightly coarser grained than the other two samples and our section is cut by a large (1 mm in width) dark brown melt vein and bound by a fusion crust. LAP 02226,25 is the smallest of the three samples and is marginally finer grained than the other two; our section is cut by small faults that are often in-filled with brown melt.

In all three stones, the major silicate phases are pyroxene and plagioclase, with minor forsteritic and fayalitic olivine and silica (Fig. 3). The pyroxenes are intergranularly distributed between the plagioclases and forsteritic olivines. Modal pyroxene contents are 58–60%, whereas plagioclase accounts for 31–32%. Fosteritic olivines are subordinate

Table 2. Representative compositional data for pyroxenes and spinels in LAP 02205, LAP 02224, and LAP 02226; nd indicates major element concentrations below the detection limit of the instrument. Pig = pigeonite, Aug = augite; Hd= Fe,Ca-rich end-members; Fs = Fe-rich end-members; M.I. Pyx = daughter pyroxene within melt inclusion; Cr = Cr-spinel; Ul = ulvöspinel. Measurement errors are estimated to be ≤1%, based on multiple measurements of NHM silicate, oxide and metal standards.

Pyroxene	02205 Pig	02205 Aug	02205 Hd	02205 Fs	02224 Pig	02224 Aug	02224 Hd	02224 Fs	02224 M.I. Pyx	02226 Pig	02226 Aug	02226 Hd	02226 Fs	Spinel 02205 Cr	02205 Ul
Major element in wt% by EMPA															
SiO_2	50.53	49.92	46.04	45.40	50.81	50.26	45.92	45.87	48.19	51.34	49.88	45.58	45.75	0.17	0.1
TiO_2	0.68	1.4	1.71	0.71	0.58	1.01	1.17	0.62	1.95	0.55	1.42	1.50	0.48	4.89	31.69
Al_2O_3	1.11	3.11	1.59	0.58	0.93	2.43	1.35	0.53	4.46	1.05	2.79	1.74	0.55	12.16	2.27
Cr_2O_3	0.41	0.95	0.04	0.02	0.30	0.90	0.03	0.02	0.35	0.36	0.74	0.00	0.01	44.26	0.78
FeO	25.23	13.27	32.29	46.61	25.83	14.69	33.59	47.59	21.69	25.31	16.64	32.44	47.67	31.28	63.89
MnO	0.40	0.27	0.39	0.57	0.42	0.21	0.36	0.55	0.36	0.45	0.27	0.32	0.66	0.29	0.29
MgO	15.78	13.47	0.49	0.33	16.47	15.54	0.66	0.46	15.95	16.20	13.47	0.33	0.17	4.33	0.17
CaO	6.01	17.68	16.95	5.57	5.49	14.98	16.87	5.45	6.92	5.66	15.47	18.23	5.38	nd	0.17
Na_2O	0.02	0.07	0.03	0.01	0.00	0.06	0.08	0.03	0.06	0.04	0.06	0.07	nd	nd	0.02
K_2O	nd	0.02	nd	0.02	nd	0.01	0.02	0.01	nd	nd	nd	0.01	nd	nd	0.01
V_2O_3	nd	nd	nd	nd	nd	nd	nd	nd	nd	nd	nd	nd	nd	0.943	nd
Total	100.17	100.16	99.51	99.82	100.83	100.08	100.05	101.12	99.92	100.95	100.73	100.20	100.66	98.32	99.39
Mg#	52.71	64.40	2.62	1.23	53.19	65.35	3.40	1.69	56.72	53.29	59.05	1.79	0.62	19.79 (Mg#)	0.48
En / 2Ti	46.06	40.06	1.58	1.07	47.17	44.98	2.10	1.48	48.20	47.01	39.70	1.05	0.54	14.77	95.41
Fs / Al	41.32	22.14	58.84	85.78	41.52	23.85	59.57	85.92	36.77	41.20	27.53	57.53	86.89	18.37	3.42
Wo / Cr	12.62	37.80	39.58	13.14	11.31	31.17	38.34	12.60	15.03	11.79	32.77	41.42	12.57	66.86	1.17
Stoichiometry based on 6 oxygen atoms (pyroxene) / **4 oxygen atoms** (spinel)															
Si	1.944	1.884	1.922	1.962	1.943	1.895	1.919	1.960	1.838	1.955	1.888	1.900	1.966	0.006	0.004
Ti (4+)	0.020	0.040	0.054	0.023	0.017	0.029	0.037	0.020	0.056	0.016	0.040	0.047	0.015	0.127	0.891
Al	0.050	0.138	0.078	0.030	0.042	0.108	0.066	0.027	0.200	0.047	0.125	0.085	0.028	0.496	0.100
Cr	0.012	0.028	0.001	0.001	0.009	0.027	0.001	0.001	0.011	0.011	0.022	0.000	0.000	1.210	0.023
Fe (2+)	0.812	0.419	1.127	1.684	0.826	0.463	1.174	1.700	0.692	0.806	0.527	1.130	1.713	0.905	1.999
Mn	0.013	0.009	0.014	0.021	0.014	0.007	0.013	0.020	0.012	0.014	0.008	0.011	0.024	0.008	0.009
Mg	0.905	0.758	0.030	0.021	0.939	0.873	0.041	0.029	0.907	0.920	0.760	0.021	0.011	0.223	0.010
Ca	0.248	0.715	0.758	0.258	0.225	0.605	0.756	0.249	0.283	0.231	0.627	0.814	0.248	0.000	0.007
Na	0.002	0.005	0.002	0.001	0.000	0.005	0.006	0.002	0.004	0.003	0.005	0.005	0.000	0.000	0.001
K	0.000	0.001	0.000	0.001	0.000	0.000	0.001	0.000	0.000	0.000	0.000	0.000	0.000	0.000	0.001
V														0.026	0.000
Sum	4.006	3.996	3.986	4.001	4.015	4.012	4.014	4.008	4.003	4.002	4.001	4.014	4.005	2.975	3.044
Tet site	1.994	2.022	2.000	1.991	1.985	2.003	1.985	1.986	2.039	2.002	2.012	1.985	1.993		
Oct site	2.011	1.974	1.986	2.010	2.030	2.009	2.029	2.022	1.964	2.000	1.989	2.029	2.011		

For the spinel (Cr, Ul) columns, the four rows listed as Mg#, En, Fs, Wo represent Mg#, 2Ti, Al, and Cr, respectively.
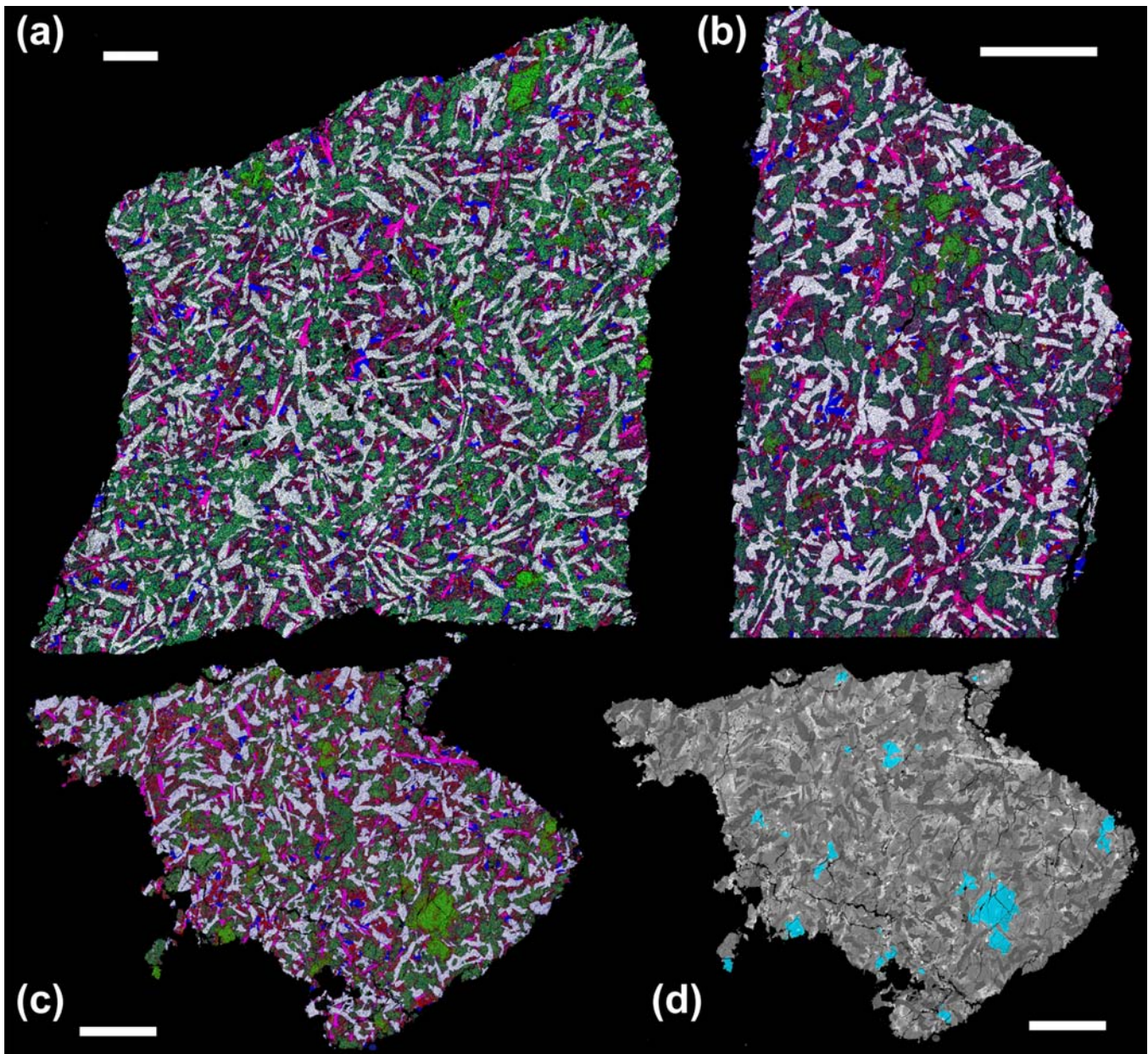
Fig. 3. False color X-ray maps of sections of a) LAP 02205,32, b) LAP 02224,35, and c) LAP 02226,25, where white represents Al (plagioclases), yellow represents Ca (plagioclase), red represents Fe (pyroxene rims and fayalitic areas), green represents Mg (pyroxene cores and forsteritic olivines), blue represents Si (cristobalite grains), and pink represents areas enriched in Ti (ilmenite and spinel). This technique particularly highlights the location of forsteritic olivine (bright green areas), fayalite (brightest red areas), ilmenite (pink), silica (blue), and plagioclase (white phases). d) The locations of forsteritic olivine are highlighted on a montaged backscattered electron image of thin section LAP 02226,25—similar phase maps were compiled for all other mineral phases. The proportional number of pixels from each identified phase is then used to calculate a mineral mode for the section (Table 5). Scale bars are 1 mm.

(modally <3%) and generally have an anhedral form subophitically enclosed by pyroxene phases. All three stones have very similar mineral proportions (Table 5), suggesting that they originated from the same lava flow.

Oxide phases include ilmenite and a group of chemically diverse spinels that ranges from titanium-chromite to ulvöspinel. Ilmenite forms about 3% and spinel phases account for <1% of the sections. Troilite and FeNi grains are dispersed through the samples, particularly associated with residual-melt regions. Mesostasis areas are composed of extremely fractionated liquid-silicate immiscible melt phases including pyroxferroite, fayalite, silica, baddelyite (ZrO_2), K-Si-rich glasses, and Si-rich glasses. Using the combined fayalite and silica modes as an approximate guide to locating mesostasis areas (Fig. 3), the stones are composed of about 0.95–2.07% residual melt.
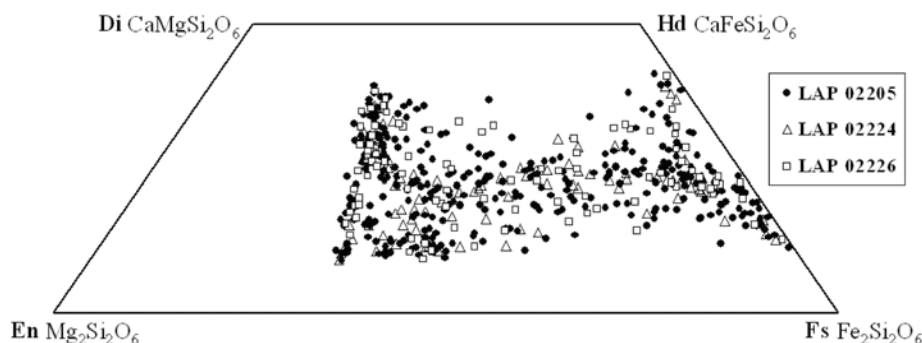
Fig. 4. Pyroxene compositions in LAP 02205,32, LAP 02224,35, and LAP 02226,25 plotted on a pyroxene quadrilateral. The three stones show very similar compositional trends with pyroxenes zoned from Mg-rich cores to Fe-rich rims. This similarity is evidence that the stones are geochemically related and are likely to have originated from the same lava flow.

Mineral Composition

Silicates

Pyroxene is the most common silicate mineral in all three stones (Tables 2 and 5), occurring as large (up to ~1 mm) grains that subophitically enclose other mineral phases. Most of the pyroxene crystals are pristine, with a small fraction showing evidence of shock deformation. The latter are heavily fractured, displaying mosaic extinction in cross-polarized light. Moreover, some crystals clearly exhibit parallel internal planar features; we interpret these as shock-induced planar deformation features (PDFs) and not exsolution lamellae, as suggested by Righter et al. (2005).

Pyroxenes show substantial variations (LAP 02205: Fs_{21-90} Wo_{9-41} En_{0-58}; LAP 02224: Fs_{23-86} Wo_{8-39} En_{1-59}; LAP 02226: Fs_{22-87} Wo_{8-40} En_{0-55}) (Fig. 4), and are nearly all gradually zoned from Mg-enriched pigeonites and subcalcic augite cores to rims that have evolved Fe-rich compositions that in extreme cases are pyroxferroitic. This zonation represents a magmatic history where pyroxene growth developed from an evolving melt that became progressively Mg-depleted with time. Melt fractionation is responsible for late-stage Fe-enrichment in pyroxenes that occur throughout the samples and in pyroxenes adjacent to mesostasis areas where grains have near-end member compositions (Fig. 4). There are a few grains that have sharper boundaries between the core (Mg-rich) and the rim (Fe-rich), which may represent a resorption effort.

Ti# (molar Ti/[Ti + Cr]) is a useful index of fractionation in pyroxenes (Nielsen and Drake 1978). Pyroxenes show a positive correlation between Ti# and Fe# (molar $Fe^{2+}/[Fe^{2+} + Mg]$) (Fig. 5a), representing a typical fractionating basalt trend. Pyroxene cores show a variation between high (subcalcic augites) and low-Ca (pigeonites) varieties, with pigeonites tending to have lower Ti# values, suggesting that Ti substituted more easily into clinopyroxenes in these early phase crystals. These trends have been observed in other basaltic/basalt-bearing lunar meteorites (Arai et al. 1996, 2002; Anand et al. 2003a) and Apollo rocks (Taylor and Misra

1975; Nielsen and Drake 1978). The cation ratio between Al and Ti in pyroxenes is a useful indicator of concurrent crystallization trends and elemental partitioning in the melt (Fig. 5b). According to mineral crystallization trends predicted by the MELTS thermodynamic modeling code (Ghiorso and Sack 1995; Asimow and Ghiorso 1998) feldspar should appear on the liquidus at about $Mg\#_{58}$ (Fig. 5b) and this is consistent with a change in slope as Al is preferentially partitioned into co-crystallizing plagioclase phases. The flattened slope from about $Mg\#_{40}$ in Fig. 5b is indicative of Ti, Mg, and Al all being extracted from the melt as pyroxene, ilmenite, and plagioclase are co-crystallizing (Nielsen and Drake 1978), consistent with our predictions made using MELTS.

Trace element compositions were measured in eight pyroxenes of different subcalcic augites and pigeonite compositions (Table 6). Concentrations are similar to those measured by Anand et al. (2006) in pyroxenes in LAP 02205,36/31 using SIMS analysis. REE concentrations in pyroxenes vary with major element composition (Fig. 6a insert). Pyroxenes 8, 6, 3, and 7, which are all subcalcic augites with >2% Al substitution, have greater concentrations of REE compared to pyroxenes 1, 4, 5, and 2, which are pigeonites with Al-substitution <1%. Pyroxenes have a range of $(La/Lu)_{cn}$ of 0.05 to 0.78 in the mineral phase, and 20.2–1.3 in the reconstructed melt and have deep negative Eu anomalies, with Eu/Eu* (i.e., $Eu_{cn}/\sqrt{(Sm_{cn} \times Gd_{cn})}$, where cn indicates chondrite-normalized) values in the range 0.14 to 0.17 (Fig. 6a). Using the trace element distribution coefficients compiled by Snyder et al. (1995), we can reconstruct the REE pattern of the original melt from which these pyroxenes crystallized, which yields Eu/Eu* values in the range of 0.18 to 0.36 (Fig. 6a). In these reconstructions, the distribution coefficients for clinopyroxenes were used for subcalcic augites/augites (3, 6, 7, and 8), and pigeonite values were used for pyroxenes 1, 2, 4, and 5. From these reconstructed melts, we can infer a pyroxene crystallization sequence of Mg-rich sub-calcic augite grains with later co-crystallizing pigeonites formed from a slightly more evolved melt that had higher REE concentrations.
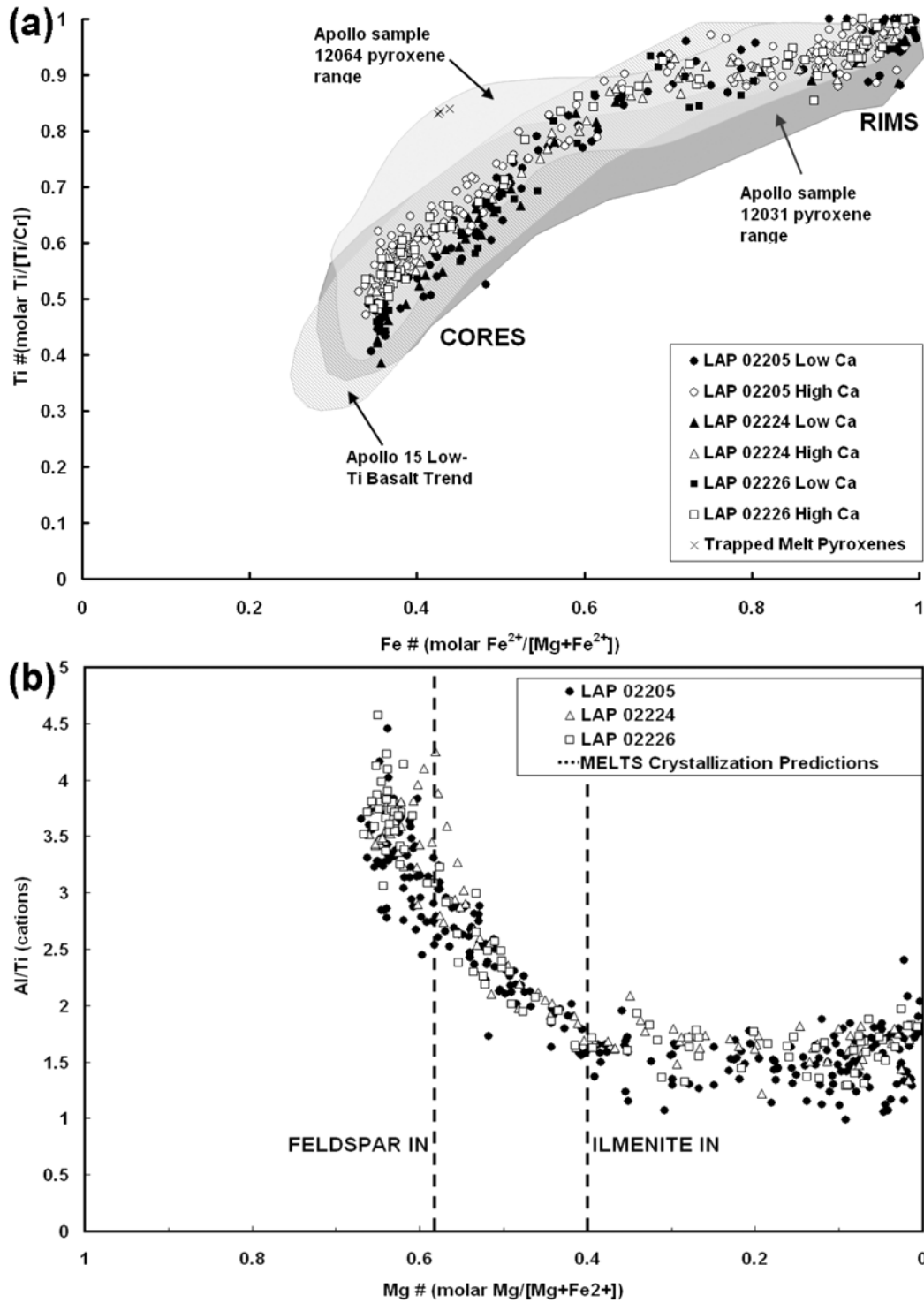
Fig. 5. a) A diagram of Ti# versus Fe# for pyroxene varieties in LAP 02205, LAP 02224, and LAP 02226 compared to similar crystallization trends seen in Apollos 15 and 12 low-Ti basalt samples (shaded regions, taken from Nielsen and Drake 1978). Open symbols represent pyroxenes with $Ca/(Ca + Mg + Fe^{2+}) > 20$ mol%; closed symbols represent <20 mol%. b) Mg# versus cation ratio of Al/Ti in pyroxenes in LAP stones. Superimposed are predictions using the MELTS thermodynamic modeling code (Ghiorso and Sack 1995; Asimow and Ghiorso 1998) of the point when feldspar ($Mg\#_{58}$) and ilmenite ($Mg\#_{40}$) appeared of the liquidus, and started to co-crystallize with pyroxene grains. These predictions correlate well with observations of a depletion in Al when plagioclase is being co-crystallized between $\sim Mg\#_{60}$ and $\sim Mg\#_{40}$, and a flattening of the trend between $\sim Mg\#_{40}$ and $\sim Mg\#_{0}$ where Ti, Al, and Mg are being partitioned into co-crystallizing respective ilmenite, plagioclase, and pyroxene phases.
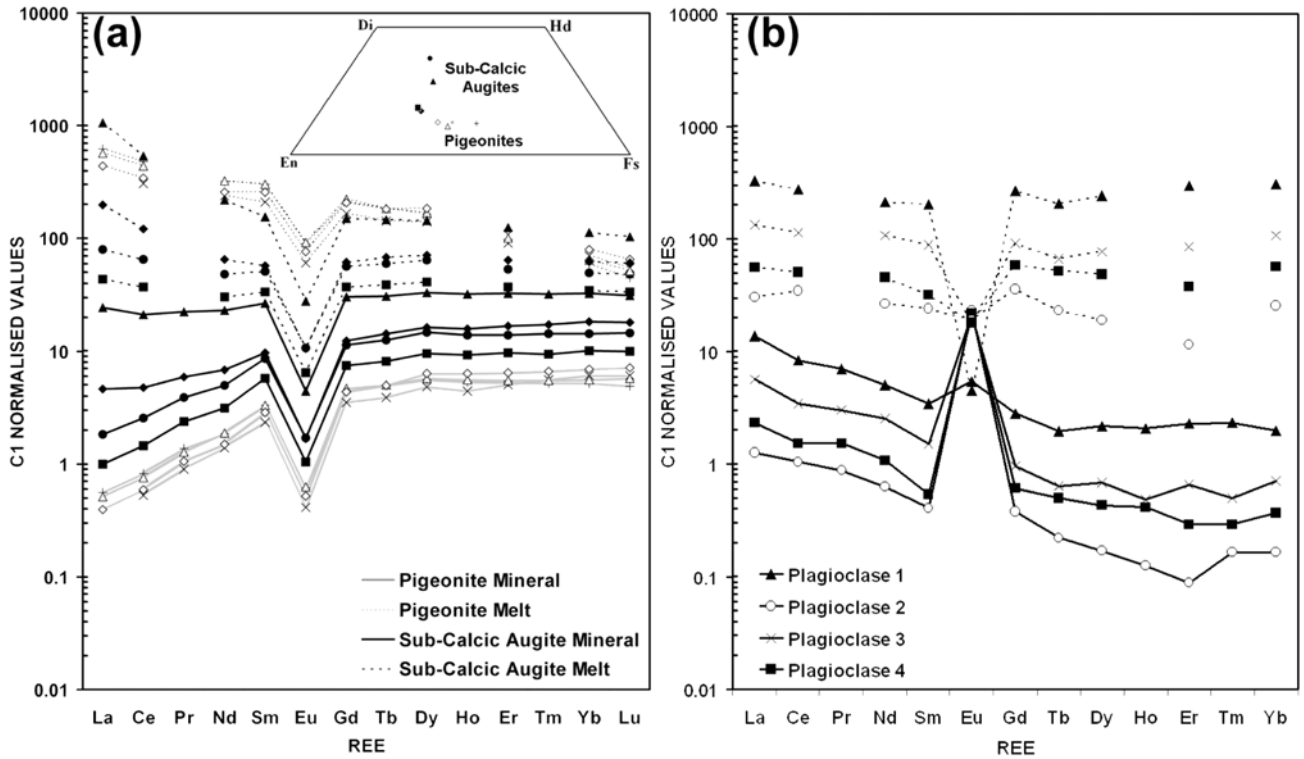
Fig. 6. a) REE composition in LAP 02205 pyroxenes with their reconstructed melt compositions (see text for details), using the lunar distribution coefficients compiled by Snyder et al. (1995) and normalized to the C1 values of Anders and Grevesse (1989). Solid lines are mineral analyses, with pigeonites in grey and subcalcic augites/augites in black. Dashed lines are their respective reconstructed melt REE concentrations. The inlaid quadrilateral shows the respective pyroxene compositions. b) REE patterns of plagioclase crystals in LAP 02205 normalized to the C1-chondrite values of Anders and Grevesse (1989). Dashed lines represent reconstructed melt REE concentrations.
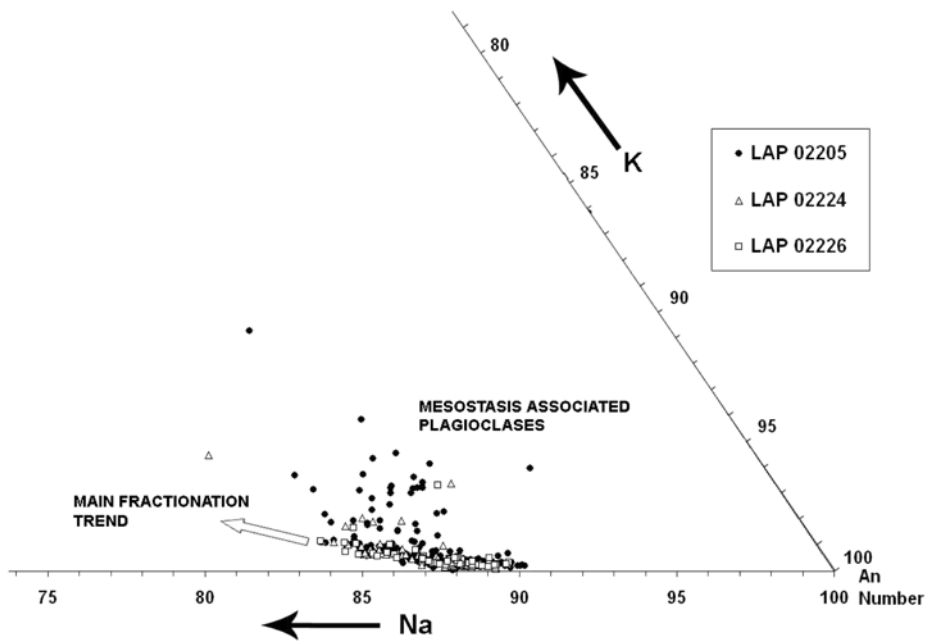

Fig. 7. A ternary plot of plagioclase content in LAP 02205,32, LAP 02224,35, and LAP 02226,25 showing a typical trend of basalt fractionation (increasing Or and Ab content with decreasing An content). K-enriched compositions that exhibit a scattered trend representing those plagioclase grains associated with mesostasis areas.

Table 3. Representative compositional data for plagioclases and olivines in LAP 02205, LAP 02224, and LAP 02226. Fo = Forstertic olivine, Fa = fayalitic olivine. Measurement errors are estimated to be ≤1%, based on multiple measurements of NHM silicate, oxide, and metal standards.

Plagioclase	02205	02205	02205	02224	02224	02224	02226	02226
	Core	Na-rim	K-rim	Core	Na-rim	K-rim	Core	Na-rim
Major element in wt% by EMPA								
SiO_2	47.86	47.95	49.23	47.72	48.90	49.26	47.19	49.42
TiO_2	0.13	0.06	0.37	0.08	0.08	0.09	0.06	0.05
Al_2O_3	31.97	31.37	30.43	32.81	31.28	30.58	32.71	31.71
Cr_2O_3	nd	nd	nd	0.04	0.03	0.02	0.03	0.00
FeO	0.82	0.95	1.67	0.61	1.00	1.80	0.58	0.93
MnO	0.01	0.06	0.04	nd	nd	nd	nd	0.07
MgO	0.22	0.09	0.02	0.18	0.12	0.03	0.31	0.13
CaO	17.44	17.01	16.33	17.95	17.08	16.82	18.01	16.87
Na_2O	1.37	1.54	1.64	1.22	1.61	1.11	1.30	1.51
K_2O	0.08	0.15	0.41	0.06	0.13	0.62	0.04	0.13
Total	99.91	99.19	100.13	100.67	100.23	100.34	100.23	100.83
An	87.17	85.13	82.58	88.78	84.77	85.93	88.25	85.40
Ab	12.38	13.95	14.97	10.88	14.49	10.28	11.50	13.80
Or	0.46	0.92	2.45	0.34	0.74	3.80	0.25	0.80
Stoichiometry based on 8 oxygen atoms								
Si	2.206	2.227	2.268	2.183	2.245	2.268	2.171	2.251
Ti (4+)	0.005	0.002	0.013	0.003	0.003	0.003	0.002	0.002
Al	1.737	1.717	1.652	1.769	1.693	1.659	1.774	1.702
Cr	0.000	0.000	0.000	0.002	0.001	0.001	0.001	0.000
Fe (2+)	0.031	0.037	0.064	0.023	0.038	0.069	0.022	0.036
Mn	0.001	0.002	0.002	0.000	0.000	0.000	0.000	0.003
Mg	0.015	0.006	0.002	0.013	0.008	0.002	0.021	0.009
Ca	0.861	0.847	0.806	0.880	0.840	0.830	0.888	0.823
Na	0.122	0.139	0.146	0.108	0.144	0.099	0.116	0.133
K	0.005	0.009	0.024	0.003	0.007	0.037	0.002	0.008
Sum	4.984	4.986	4.978	4.984	4.980	4.967	4.998	4.966
Tet site	3.944	3.944	3.921	3.953	3.938	3.927	3.945	3.954
Oct site	1.040	1.042	1.057	1.031	1.042	1.041	1.053	1.013

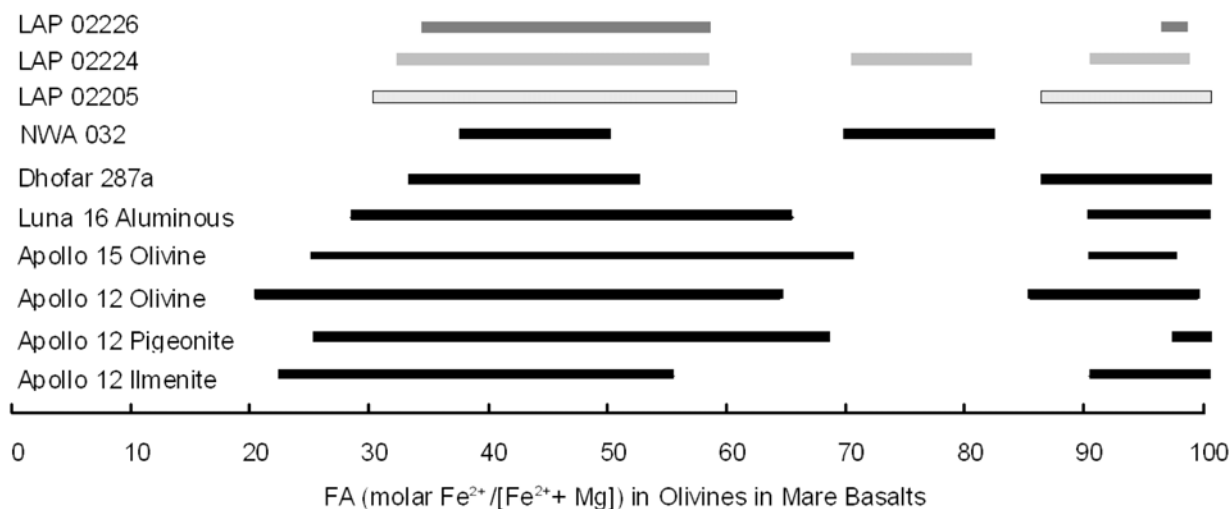| Olivine	02205	02205	02224	02224	02226	02226
	Fo	Fa	Fo	Fa	Fo	Fa
Major element in wt% by EMPA						
SiO_2	36.24	29.02	36.58	29.30	36.97	29.30
TiO_2	0.03	0.13	0.06	0.15	0.06	0.13
Al_2O_3	0.05	0.07	0.03	0.05	0.06	0.02
Cr_2O_3	0.28	nd	0.22	nd	0.18	0.01
FeO	30.71	68.28	33.15	68.78	30.06	68.65
MnO	0.28	0.70	0.31	0.70	0.28	0.62
MgO	31.64	0.62	30.64	1.06	33.11	0.20
CaO	0.37	0.75	0.38	0.74	0.34	1.02
Na_2O	nd	0.05	0.04	nd	0.01	nd
K_2O	nd	0.05	0.00	nd	nd	nd
Total	99.60	99.66	101.40	100.77	101.06	99.95
Mg#	64.74	1.59	62.23	2.66	66.25	0.52
Fe#	35.26	98.41	37.77	97.34	33.75	99.48
Stoichiometry based on 4 oxygen atoms						
Si	0.990	0.985	0.991	0.982	0.990	0.992
Ti (4+)	0.001	0.003	0.001	0.004	0.001	0.003
Al	0.002	0.003	0.001	0.002	0.002	0.001
Cr	0.006	0.000	0.005	0.000	0.004	0.000
Fe (2+)	0.702	1.938	0.751	1.927	0.673	1.944
Mn	0.006	0.020	0.007	0.020	0.006	0.018
Mg	1.288	0.031	1.237	0.053	1.321	0.010
Ca	0.011	0.027	0.011	0.027	0.010	0.010
Na	0.000	0.003	0.002	0.000	0.000	0.037
K	0.000	0.002	0.000	0.000	0.000	0.000
Sum	3.006	3.013	3.006	3.014	3.007	3.004

Fig. 8. A comparison of olivine Fe# (molar Fe/ [Fe + Mg]) compositions in LAP 02205, LAP 02224, and LAP 02226 compared to mare basalt olivine compositions (Papike et al. 1991) and basaltic lunar meteorite Dhofar 287a (Anand et al. 2003b) and NWA 032 (Anand et al 2006). LAP lunar stones show a similar range to Apollo 12 and 15 basalts, albeit with a higher Fe# value for the most primitive forsterites. LAP 02224 shows an intermediate range of olivine chemistries which correspond to the Fe-rich rims of large olivine crystals.

Plagioclase varies from being fractured with relict twinning, to <40% having a glassy appearance caused by shock-induced vitrification (maskelynization). It typically occurs as lath-shaped subhedral grains (typically 50–800 μm) that crystallized relatively slowly and cotectically with pyroxene phases. Plagioclases have complex compositional variations (LAP 02205: An_{91-81}; LAP 02224: An_{90-84}; LAP 02205: An_{90-84}; Fig. 7). Grains that are adjacent to mesostasis areas and associated with residual melt crystallization have a higher Or# (molar K/[Ca + K + Na]) and Ab# (molar Na/[Ca + K + Na]) content (Fig. 7; Table 3) typical of lunar basalt fractionation trends. Rare earth element concentrations were measured in the cores of four large (>500 μm) plagioclase crystals (Fig. 6b; Table 6). Concentrations agree well with those reported by Anand et al. (2006) for plagioclases grains. The grains analyzed trend from high LREE to lower HREE with a range of $(La/Lu)_{cn}$ from 11.2 to 5.5, and have large positive Eu anomalies (Eu/Eu^* in the range 8.9 to 25.7). The reconstructed pyroxene (Fig. 6a) and plagioclase (Fig. 6b) melt REE concentrations clearly show that there was co-crystallization between these two main mineral phases.

Olivine in LAP falls into two main groups (Table 3; Fig. 8). Forsteritic varieties range from large grains (200 μm–1 mm) to smaller anhedral grains (40–100 μm). Some of the larger varieties are zoned from relatively Mg-rich (Fo_{64}–Fo_{46}) core compositions to narrow (<100 μm) Fe-rich rims (Fig. 9a). This Fe-rich rim structure is often incomplete or missing, causing an undulatory contact with surrounding pyroxene phases, indicating that the olivine grains underwent partial resorption to form pyroxene phases during melt cooling. Anhedral, fayalitic (Fa_{87-100}) varieties form part of the groundmass of the mesostasis regions. Olivines in the stones show a similar compositional range to that in Apollo mare basalt samples and lunar basaltic meteorites (Fig. 8).

A few (<5%) large forsteritic olivine grains (Fig. 9) contain subrounded multiphase inclusions that have sharp boundaries with their host. The melt inclusions contain daughter minerals that include a glass phase (rich in Al and Ca) with microcrysts of a Ti-rich opaque phase intergrown with barred and feathery aggregates (<5 μm) of pseudo-pyroxene glass (Figs. 9b and 9c) and microcrysts (10–20 μm) of near-stiochiometric pyroxene composition (Table 2). These phases nucleated from the contact with the olivine where there is a boundary pyroxene layer. These are not an injected melt product, which would be expected to be present in the surrounding fractures and cracks, but are likely to be a primary melt inclusion that was trapped when the olivine crystallized. Similar inclusions have also been observed in olivines from 02224 (Fig. 9c), 02226, and in other sections of LAP (Righter et al. 2005). These areas are texturally similar to trapped melt areas measured in Apollo 12 and 15 mare basalt samples (as discussed in Weiblen 1977), and NWA 032 (Fagen et al. 2002), suggesting that this process is typical of lunar low-Ti melt conditions.

Fayalite grains are common and all are associated with the mesostasis regions of the samples. These masses are anhedral and form a groundmass containing Al, K-enriched glasses, silica, troilite blebs, plagioclases, Fe-rich pyroxenes, and ilmenite. It has been suggested (Aramovich et al. 2001; Fagen et al. 2002) that these late-stage olivines could be formed in the breakdown of pyroxferroite at low pressure into a stable of assemblage of hedenbergite-fayalite-SiO_2. There is evidence for this process in all three stones from the observation of SiO_2 within, and stable pyroxenes adjacent to, the mesostasis regions.
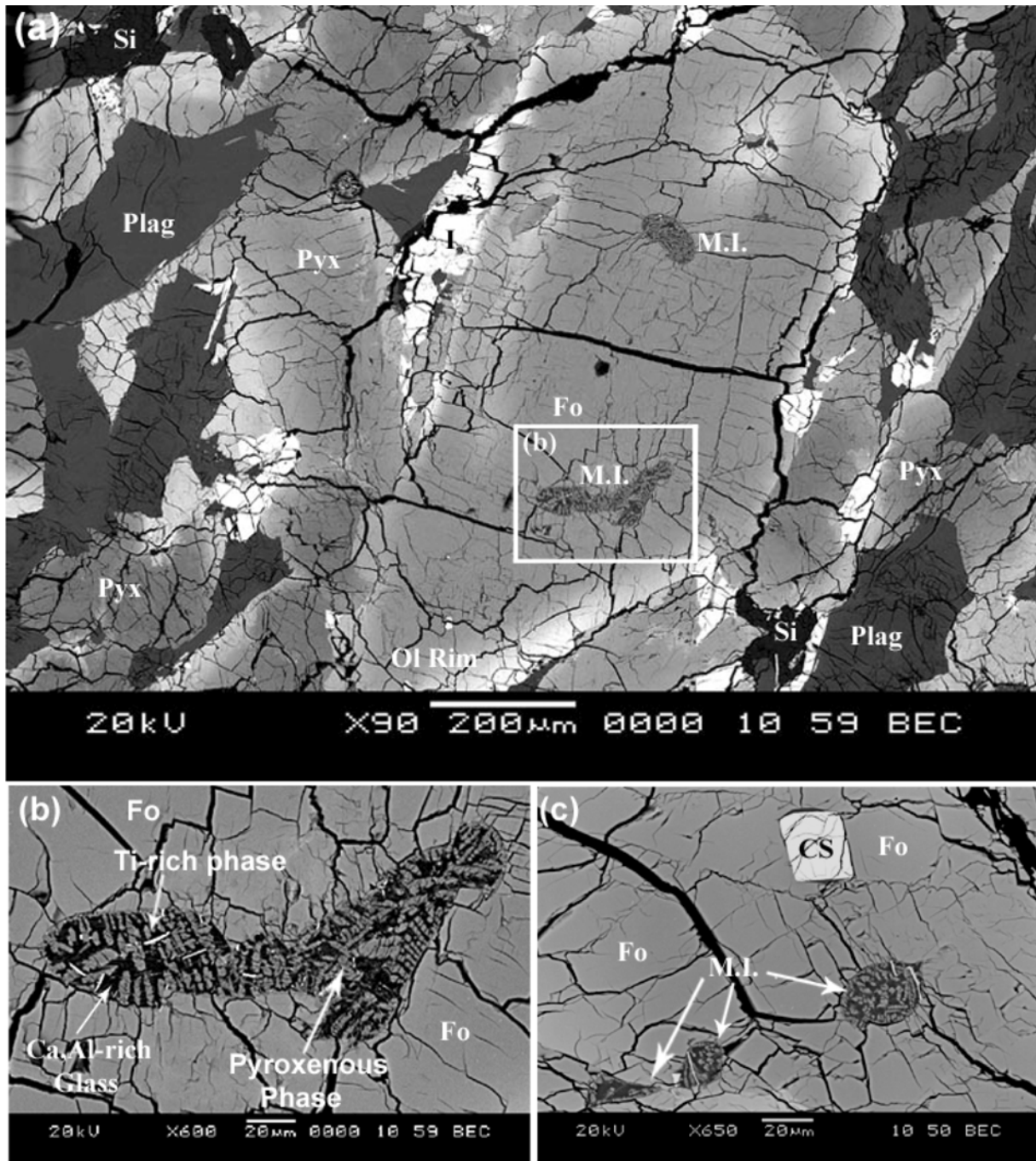
Fig. 9. a) A BSE image of a large olivine grain in LAP 02205. The mineral is zoned from Fo_{63} core to Fo_{39} rims and contains two small quenched melt areas that have been highlighted. b) A close-up of the trapped melt with microcrystalline texture in LAP 02205 where daughter barred pyroxene microcrysts sit in a glassy matrix with micro inclusions of a Ti-rich and small S-rich phases (bright albedo). c) A close-up of small trapped melt inclusions in a single olivine in LAP 02224. Minerals are represented by the following symbols: Pyx = pyroxene, Plag = plagioclase, I = ilmenite, Fo = forsteritic olivine, CS = chromite-spinel, MI = melt inclusion, Si = silica, and Ol Rim = olivine rim.

Oxides

Ilmenite (~3% by mode) is the most common oxide in LAP 02205, 02224, and 02226 and occurs as euhedral elongate crystals (typically 100–800 µm) distributed interstitally throughout each sample and as more subhedral-anhedral masses (typically <150 µm) in mesostasis regions.

Ilmenite crystals in the three stones contain <0.4% MgO, 0.25–0.45% MnO, and <0.5% Cr_2O_3. The amount of Mg-substitution is generally lower than in other low-Ti Apollo and Luna mare basalt suites but is similar to compositions in Apollo 12 pigeonite and olivine basalts (Papike et al. 1991). All three stones show a very similar ilmenite major and minor
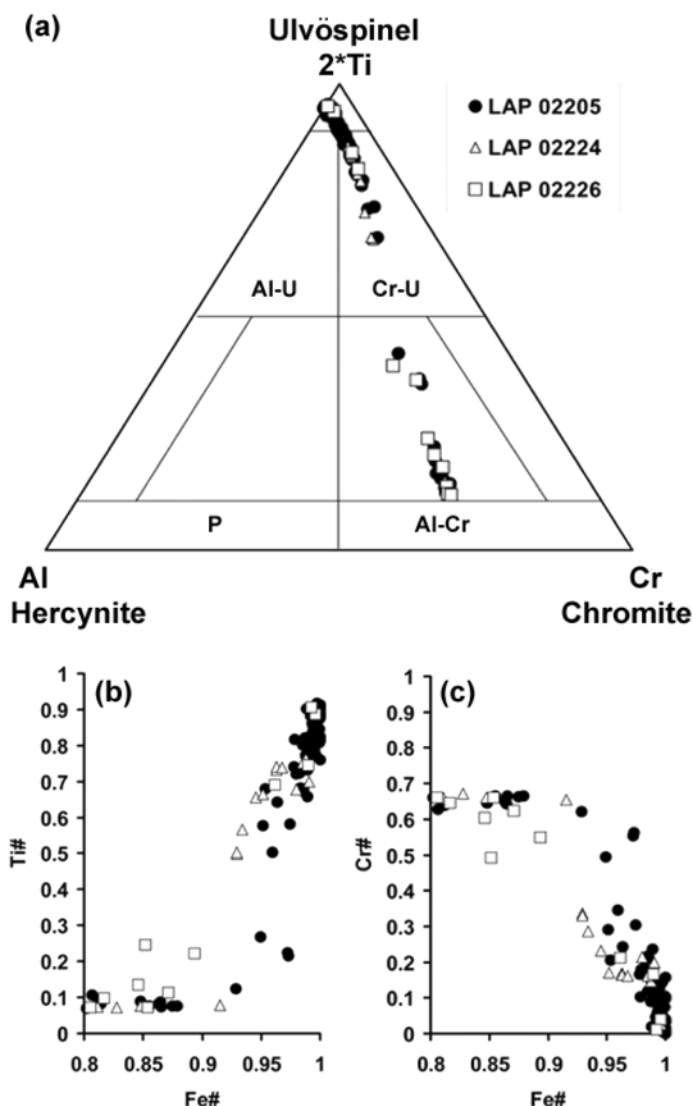
Fig. 10. a) A compositional diagram (2Ti-Cr-Al in mol%) for spinels analyzed in LAP 02205, LAP 02224, and LAP 02226. Compositions zones: P = picotite, Al-Cr = aluminous chromite, Al-U = aluminous ulvöspinel, Cr-U = chromian ulvöspinel. b) A plot of Fe# (molar Fe^{2+}/ [Fe^{2+} + Mg]) versus Ti# (molar Ti/[Ti + Cr + Al]). c) Fe# versus Cr# (molar Cr/ [Al + Cr]) showing crystallization trend of spinels in LAP 02205. Symbols are the same in all three plots.

element composition that is further evidence that the stones originate from the same melt source on the Moon.

Spinel is the second most abundant oxide mineral in LAP (0.3–1% by mode). Small Cr-rich spinel (Al-Ti-chromite) grains are found as inclusions within forsteritic olivine grains and are related to early crystallization processes. These are enriched in Mg ($Mg\#_{3-25}$) compared to the late stage ulvöspinel grains ($Mg\#_{0-2}$; Table 2). Interstitial spinels follow a narrow fractionation trend (Fig. 10a) with an increase in Cr-content/decrease in Ti-content, evolving to ulvöspinel compositions that are often associated with mesostasis area.

Some of the grains display zonation from small Al-Ti-chromite-rich cores to sharply defined chromium-ulvöspinel rims. The sharp increase in TiO_2, with a moderate increase in Fe# and a decrease in Cr_2O_3 and Al_2O_3 (Figs. 10b and 10c),

represents the "second" type of spinel zonation as discussed by El Goresy et al. (1976), where early crystallized spinels reequilibrated with crystallizing melt. Thus the chromite spinels form nucleation cores for later precipitated evolved ulvöspinels. The compositional gap (Fig. 10a) between the Cr-rich and Cr-Ti-rich spinels has been interpreted by previous investigators (Arai et al. 1996; Jolliff et al. 2003) to be the result of partial resorption of titian-chromite when melt cooling rates are moderately slow.

The spinel compositions (Fig. 10a) and the Fe# and Ti# trends (Figs. 10b and 10c) are similar to the fractionation trends in some Apollo 12 and Apollo 15 low-Ti basalts (Papike et al. 1991, Anand et al. 2003b), and also those in low-Ti meteorites Yamato-793169 (Arai et al. 1996) and Dhofar 287a (Anand et al. 2003b). The LAP stones, however,

Table 4. Representative average composition of accessory phases, melt veins, and fusion crust. Units are wt%. Errors are standard deviation based on the number of spots analyzed. Melt vein (M.V.) average generated from 17 spots in single melt vein. Fusion crust average generated from 11 spatially diverse spots within crust melt region.

	02205 Ilmenite	02224 Ilmenite	02226 Ilmenite	02205 Cristobalite	02205 Si-K glass	02224 M.V. average	02224 Fusion crust
Number of spots	78	38	25	24	13	17	11
Major element in wt% by EMPA							
SiO_2	0.05 ± 0.04	0.04 ± 0.02	0.04 ± 0.03	99.52 ± 1.07	79.61 ± 1.85	44.77 ± 0.31	45.28 ± 3.39
TiO_2	52.68 ± 5.08	52.92 ± 0.34	52.71 ± 0.33	0.26 ± 0.05	0.56 ± 0.06	3.23 ± 0.16	2.91 ± 0.77
Al_2O_3	0.14 ± 0.07	0.14 ± 0.03	0.16 ± 0.03	0.73 ± 0.14	11.93 ± 0.64	11.83 ± 0.25	6.95 ± 2.52
Cr_2O_3	0.11 ± 0.07	0.19 ± 0.10	0.16 ± 0.09	0.01 ± 0.01	0.01 ± 0.01	0.30 ± 0.05	0.32 ± 0.22
FeO	46.21 ± 4.46	47.00 ± 0.61	46.88 ± 0.65	0.01 ± 0.01	0.01 ± 0.02	20.81 ± 0.94	25.74 ± 7.36
MnO	0.34 ± 0.05	0.34 ± 0.04	0.32 ± 0.04	0.01 ± 0.01	0.02 ± 0.02	0.25 ± 0.03	0.31 ± 0.06
MgO	0.06 ± 0.17	0.28 ± 0.33	0.18 ± 0.29	nd	0.01 ± 0.01	7.00 ± 0.56	7.36 ± 3.36
CaO	0.10 ± 0.08	0.10 ± 0.05	0.10 ± 0.05	0.21 ± 0.05	1.06 ± 0.36	11.22 ± 0.19	11.02 ± 1.96
Na_2O	0.02 ± 0.02	0.01 ± 0.02	0.02 ± 0.02	0.14 ± 0.04	0.24 ± 0.06	0.46 ± 0.04	0.24 ± 0.12
K_2O	0.01 ± 0.01	0.01 ± 0.01	0.01 ± 0.01	0.03 ± 0.02	5.42 ± 0.58	0.13 ± 0.02	0.09 ± 0.05
P_2O_5	0.02 ± 0.02	0.02 ± 0.03	0.02 ± 0.02	nd	0.14 ± 0.05	0.14 ± 0.04	0.12 ± 0.08
NiO	0.02 ± 0.02	0.01 ± 0.02	0.02 ± 0.02	nd	nd	0.02 ± 0.02	0.01 ± 0.01
Total	99.76	101.06	100.62	100.96	99.02	100.17	100.34
Mg#						37.52	33.78

	02205 Hi-Ni metal	02205 Low-Ni metal	02205 Troilite
Number of spots	3	2	30
Major element in wt% by EMPA			
Si	0.04 ± 0.01	nd	0.04 ± 0.03
Ti	0.33 ± 0.01	0.13 ± 0.11	0.09 ± 0.09
Cr	0.30 ± 0.01	0.23 ± 0.10	0.01 ± 0.01
Fe	68.85 ± 0.95	86.68 ± 2.23	62.89 ± 1.14
Mn	0.03 ± 0.01	0.02 ± 0.02	0.02 ± 0.01
P	0.01 ± 0.01	nd	0.01 ± 0.02
Ni	26.20 ± 0.40	8.15 ± 2.07	0.03 ± 0.04
S	0.02 ± 0.01	0.08 ± 0.06	35.86 ± 0.52
Zn	nd	nd	0.02 ± 0.02
Co	3.73 ± 0.05	1.91 ± 0.61	0.04 ± 0.02
Total	99.52	97.21	99.01

have more evolved (Ti-rich) ulvöspinel compositions than most Apollo samples and Dhofar 287a, another indication that LAP crystallized from a comparatively evolved melt. The three LAP stones have very similar spinel fractionation trends, providing further strong evidence that the stones are petrologically related.

Accessory Minerals

Silica occurs in all three stones, either as anhedral small crystals (<0.3 mm) in the groundmass or, more frequently, as small grains or blebs intergrown with Al-rich glass and hosted by fayalite in the mesostasis. Silica in LAP 02205 often contains minor contaminants of Na_2O (0.05–0.22 wt%), Al_2O_3 (≤1.45%), K_2O (≤0.22%), and FeO (0.14–0.79%). The presence of conchoidal fractures as a result of relatively rapid inversion from a high to a low temperature structure indicates that the silica phase is cristobalite. On the basis of modal mineralogy, silica occurs as 0.38% of LAP 02205, as 0.59% of LAP 02224, and 0.45% of LAP 02226. The presence of free silica indicates that the LAP melt was silica oversaturated.

Sulfide grains (Table 4) in LAP are ubiquitously troilite (FeS). Small blebs (<5 μm) occur dispersed within pyroxene crystals, but larger grains (<80 μm) occur adjacent to, or within, mesostasis. This suggests that sulphur was concentrated in the residual melt. Metal grains in the form of FeNi (Table 4) are rare, tiny (≤5 μm), anhedral blebs and are distributed in late-stage pyroxene phases and adjacent to plagioclase rims, also suggesting formation as a late-stage melt product in a low (iron-wustite; IW) oxygen fugacity environment (Taylor and Day 2005).

Mesostasis

Mesostasis is a common feature of the Apollo mare basalt suite collection (e.g., Roedder and Weiblen 1977; Papike et al. 1998) and has been observed in basaltic lunar meteorites (Anand et al. 2003b; Jolliff et al. 2003). The LAP stones contain mesostasis aggregates (typically <500 μm) (Fig. 11a), which have a typical fayalite, cristobalite, and plagioclase mineralogy associated with eutectic crystallization from a Fe-rich residual melt with an enriched REE concentration. They are irregular in shape, occurring interstitially between large plagioclase and pyroxene crystals. Typically, mesostasis regions have a diagnostic texture of glass blebs (<5 μm) enclosed by a fayalitic groundmass (Fig. 11a) and are often associated with ilmenite, troilite, spinel, pyroxferroite, larger glass masses, silica, baddelylite blebs, and K-rich plagioclase. Typically, the pyroxenes surrounding the mesostasis are Fe-rich, indicating that they too are late-stage crystallization products. The mesostasis areas are highly enriched in incompatible trace elements (ITE) (Table 6), containing up to ~600 × C1-chondrite concentrations for most REE and with a negative Eu anomaly. Glass bleb inclusions within the fayalitic groundmass

Table 5. Estimated modal mineral analysis for the three LAP stones. "Other" includes melt veins, metal, glass, and troilite. The number of pixels analyzed in each case is also given (1E+6 is 1,000,000).

	02205	02224	02226
Fayalite	1.69	0.67	0.5
Forsterite	1.4	2.71	2.76
Pyroxene	59.75	57.93	58.32
Plagioclase	32.04	31.78	32.57
Silica	0.38	0.59	0.45
Ilmenite	2.74	3.25	2.85
Spinels	0.29	0.97	0.27
Other	1.72	2.1	2.27
No. of pixels	5.77E+6	7.08E+6	1.28E+7

represent extreme magmatic fractionation; such evolved glass varieties are essentially the products of the granitic melt portion formed by liquid immiscibility. These form when the melt fractionates to about 95–98% and divided into granitic (K-enriched) (Table 4) and ferrobasaltic (REEP) fractions (Neal and Taylor 1989). The granitic glass blebs have a range in K_2O contents from 2.3 to 6.3% (Table 4).

Fusion Crust

As previously reported by Joy at al. (2005a) and Day et al. (2005, 2006), LAP 02224 has a vesicular fusion crust (Fig. 11c) caused by ablation melting and degassing of the rock's surface as it passed through the Earth's atmosphere. This is the first example of a vesicular fusion crust that has been reported for mare basalt meteoritic material and provides evidence that the sample accumulated solar-wind-implanted volatiles in the lunar near-surface environment that have exsolved upon remelting (Korotev et al. 2005). This suggests that LAP must have been part of a lava flow that was exposed at or near the lunar surface for a significant proportion of its history, allowing the penetration of solar gases. Recent Re-Os isotopic studies (Day et al. 2005) and radionuclide studies (Nishiizumi et al. 2006) of the fusion crust have attempted to constrain the exposure history of the LAP meteorite. Nishiizumi et al. (2006) report elevated [26]Al concentrations in the fusion crusts of LAP 02205 and LAP 02224, providing evidence for solar cosmic ray interaction while the rock was in situ on the lunar surface. This confirms a near-surface residence history, as suggested by the presence of a vesicular fusion crust.

We note that the average composition of this fusion crust melt (Table 4) in LAP 02224 is unexpectedly depleted in Al_2O_3, and enriched in FeO, compared to the bulk sample and melt vein average composition. This difference highlights the problem of using average fusion crust compositions to represent bulk rock composition (as also pointed out by Day et al. 2006), and is presumably due to different minerals being affected differently by the melting associated with fusion crust formation.

Table 6. Concentrations (in ppm) of REE in minerals as measured by LA-ICP-MS. Errors are based on the standard deviation of four NIST-612 synthetic standard measurements. These data are shown in Fig. 6. Pig = pigeonite, SC AUG = subcalcic augites, Plag = plagioclase, and M = mesostasis bulk area.

	Pig	Pig	Pig	SC Aug	Pig	SC Aug	SC Aug	SC Aug
La	0.13 ± 0.01	0.24 ± 0.02	0.12 ± 0.01	0.43 ± 0.04	0.09 ± 0.01	1.08 ± 0.09	0.23 ± 0.02	5.74 ± 0.47
Ce	0.50 ± 0.05	0.32 ± 0.03	0.45 ± 0.04	1.54 ± 0.14	0.36 ± 0.03	2.85 ± 0.26	0.87 ± 0.08	12.69 ± 1.16
Pr	0.12 ± 0.01	0.08 ± 0.01	0.11 ± 0.01	0.35 ± 0.03	0.09 ± 0.01	0.53 ± 0.05	0.21 ± 0.02	1.99 ± 0.17
Nd	0.84 ± 0.07	0.63 ± 0.05	0.85 ± 0.07	2.26 ± 0.18	0.68 ± 0.05	3.08 ± 0.25	1.42 ± 0.12	10.33 ± 0.84
Sm	0.49 ± 0.05	0.34 ± 0.03	0.49 ± 0.05	1.27 ± 0.12	0.42 ± 0.04	1.42 ± 0.13	0.84 ± 0.08	3.88 ± 0.37
Eu	0.03 ± 0.01	0.02 ± 0.01	0.04 ± 0.01	0.10 ± 0.01	0.03 ± 0.01	0.09 ± 0.01	0.06 ± 0.01	0.25 ± 0.02
Gd	0.87 ± 0.08	0.69 ± 0.06	0.92 ± 0.08	2.21 ± 0.20	0.86 ± 0.08	2.42 ± 0.22	1.45 ± 0.13	5.91 ± 0.54
Tb	0.18 ± 0.02	0.14 ± 0.01	0.18 ± 0.02	0.46 ± 0.04	0.18 ± 0.02	0.52 ± 0.05	0.30 ± 0.03	1.11 ± 0.10
Dy	1.36 ± 0.13	1.16 ± 0.11	1.40 ± 0.13	3.58 ± 0.33	1.53 ± 0.14	3.95 ± 0.37	2.30 ± 0.21	8.04 ± 0.75
Ho	0.30 ± 0.03	0.25 ± 0.02	0.31 ± 0.03	10.78 ± 0.07	0.35 ± 0.03	0.88 ± 0.08	0.51 ± 0.05	1.78 ± 0.16
Er	0.84 ± 0.08	0.80 ± 0.08	0.88 ± 0.08	2.20 ± 0.21	1.02 ± 0.10	2.66 ± 0.25	1.52 ± 0.14	5.19 ± 0.49
Tm	0.13 ± 0.01	0.14 ± 0.01	0.13 ± 0.01	0.35 ± 0.03	0.16 ± 0.02	0.42 ± 0.04	0.23 ± 0.02	0.78 ± 0.07
Yb	0.84 ± 0.08	0.99 ± 0.09	0.91 ± 0.08	2.32 ± 0.21	1.12 ± 0.10	2.96 ± 0.27	1.63 ± 0.15	5.32 ± 0.49
Lu	0.12 ± 0.01	0.15 ± 0.01	0.14 ± 0.01	0.35 ± 0.04	0.17 ± 0.02	0.44 ± 0.04	0.24 ± 0.02	0.75 ± 0.08

|	Plag	Plag	Plag	M1	Plag	M2
La	3.23 ± 0.26	0.30 ± 0.02	1.32 ± 0.11	51.82 ± 4.22	0.55 ± 0.04	126.83 ± 10.33
Ce	5.01 ± 0.46	0.63 ± 0.06	2.06 ± 0.19	128.31 ± 11.74	0.92 ± 0.08	302.63 ± 27.69
Pr	0.62 ± 0.05	0.08 ± 0.01	0.27 ± 0.02	17.94 ± 1.54	0.14 ± 0.01	47.16 ± 4.05
Nd	2.27 ± 0.18	0.29 ± 0.02	1.15 ± 0.09	89.19 ± 7.23	0.49 ± 0.04	249.98 ± 20.27
Sm	0.51 ± 0.05	0.06 ± 0.01	0.22 ± 0.02	28.78 ± 2.72	0.08 ± 0.01	82.55 ± 7.81
Eu	0.30 ± 0.03	1.29 ± 0.13	1.19 ± 0.12	2.85 ± 0.28	1.22 ± 0.12	7.37 ± 0.73
Gd	0.55 ± 0.05	0.07 ± 0.01	0.19 ± 0.02	37.85 ± 3.47	0.12 ± 0.01	109.53 ± 10.04
Tb	0.07 ± 0.01	0.01 ± 0.001	0.02 ± 0.002	6.62 ± 0.58	0.02 ± 0.002	19.29 ± 1.69
Dy	0.52 ± 0.05	0.04 ± 0.004	0.17 ± 0.02	46.50 ± 4.31	0.11 ± 0.01	134.70 ± 12.48
Ho	0.12 ± 0.01	0.01 ± 0.001	0.03 ± 0.002	9.66 ± 0.87	0.02 ± 0.002	28.30 ± 2.55
Er	0.36 ± 0.03	0.01 ± 0.001	0.10 ± 0.01	27.08 ± 2.57	0.05 ± 0.004	80.02 ± 7.60
Tm	0.06 ± 0.01	0.004 ± 0.001	0.01 ± 0.001	3.96 ± 0.37	0.01 ± 0.001	11.83 ± 1.12
Yb	0.32 ± 0.03	0.03 ± 0.002	0.11 ± 0.01	25.67 ± 2.37	0.06 ± 0.01	77.23 ± 7.13
Lu	0.06 ± 0.01	0.01 ± 0.001	0.01 ± 0.001	3.59 ± 0.36	0.01 ± 0.001	11.13 ± 1.13
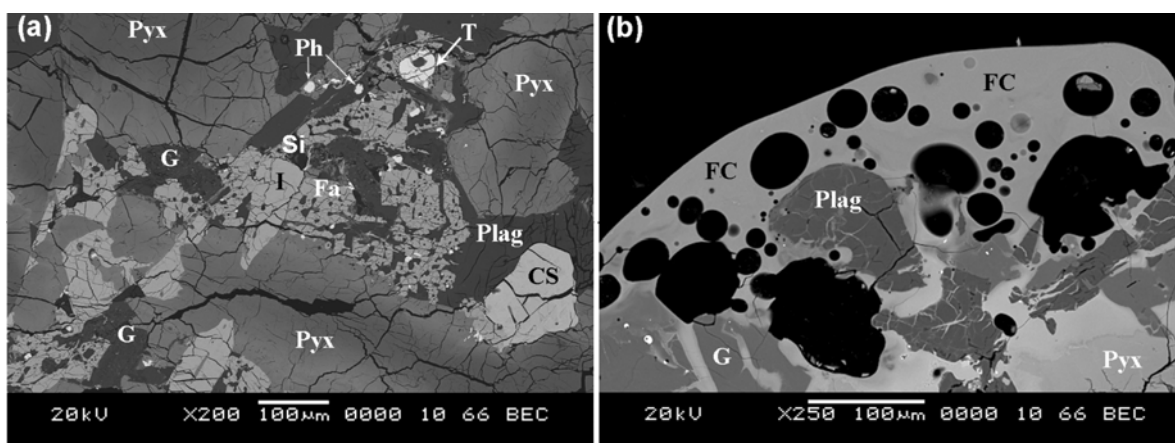
Fig. 11. a) A BSE image of a mesostasis area in LAP 02205. Bleb-like glass pockets are enclosed by fayalite groundmass and larger glass-rich regions. Mesostasis products are enclosed by Fe-rich pyroxenes, ilmenites, and plagioclase crystals. b) A BSE image of the fusion crust of LAP 02224.The vesicular grey area at top of section is the fusion crust; minerals being melted into this zone can be seen at the bottom of this zone. Vesicles (black circular regions) are heterogeneously distributed throughout the melted/melting area. Dark grey minerals are plagioclases, pale grey at the base of the image are pyroxenes, and small bright white blebs are troilite. Minerals are represented by the same symbols in Fig. 9. Fa = fayalite, T = troilite, G = glass, Ph = phosphates, and FC = fusion crust.

Shock Effects

The Moon has been subjected to intense bombardment by comets and meteorites throughout its history (Wilhelms 1987), and the effects of these impacts can clearly be seen in lunar rocks (e.g., Ryder 1985; Bischoff et al. 1998; Korotev 1991; Anand et al. 2003b). LAP 02205, 02224, and 02226 are all crystalline basalts with no evident brecciation. However, all three samples have small pockets, fractures, and faults that are partially infilled with black glass, suggesting localized intense shock pressures of greater than 60 GPa (Rubin et al. 1997). An average of 17 melt vein analyses (Table 4) is similar to those melt vein compositions reported by Righter et al. (2004) and is of pseudo-bulk rock composition. These regions are therefore interpreted as being derived from localized melting of the basalt. Minerals in LAP have been affected by different degrees of shock metamorphism, even though they were emplaced in close proximity to each other. Pyroxene grains typically display undulatory extinction with some crystals having weak mosaicism and others displaying shock-induced twinning and planar deformation features (10–30 GPa) (Rubin et al. 1997). Forsteritic olivine grains contain irregular fractures, and occasionally show undulose extinction, suggesting processes of up to S2–3 shock pressures (i.e., >10 GPa; Stöffler et al. 1991). Plagioclase grains vary in the extent of shock alteration from mildly shocked grains that display clear relict twinning, to those that have undulatory extinction and those that have no internal twinning features and are nearly isotropic in cross-polarized light. The latter implies some degree of conversion to a glass phase (maskelynization), with shock pressures greater than S5 (30–45 GPa) (Stöffler et al. 1991). The range of shock metamorphism identified is therefore likely to represent shock pressures that vary from approximately 10 GPa to >60 GPa throughout the sample.

DISCUSSION

Comparison to Other Mare Basalts

It is important to place the LAP basalt within the framework of the Apollo and Luna collections, so that petrological and geochemical comparisons can be made and relationships established between site-sampled material and randomly launched meteorites. The LAP stones are important samples because together they are only one of a few lunar meteorites to be classified as mare basalt. Others include Yamato-793169 and Asuka-881757 (Arai et al. 1996), Dhofar 287a (Anand et al. 2003b), and NWA 032/479 (Fagan et al. 2002). A pairing relationship between the LAP stones and NWA 032 has been proposed on the basis of similar mineral and bulk rock compositions (e.g., Koizuni et al. 2005; Righter et al. 2005; Zeigler et al. 2005; Anand et al. 2006). If they are source-related, LAP represents a portion of the melt that has undergone more fractionation than NWA 032 and that cooled more slowly (as it has a larger grain size). Similar young crystallization ages of NWA 032 (Ar-Ar: 2.800 ± 0.020 Ga [Fagan et al. 2002]) and LAP 02205 (Ar-Ar: 2.95 ± 0.020 Ga [Nyquist et al. 2005]; Rb/Sr: 2.956 ± 0.014 Ga [Rankenburg et al. 2005]; U/Pb: 2.929 ± 0.015 Ga [Anand et al. 2006]) help to support these pairing relationships, suggesting that they are examples of the same young mare lava that have undergone slightly different fractionation and cooling histories.

Figure 12 summarizes the classification of LAP 02205 and LAP 02225 compared to a wide range of Apollo and Luna samples. Figure 12b indicates that LAP stones fall toward the Al-rich end of the low-Ti, low-Al classification of Neal and Taylor (1992), and are most similar to the basalts in the Apollos 12 and 15 collections (Rhodes et al. 1973, 1977; Vaniman et al. 1991; Neal et al. 1994a; Papike et al. 1998).
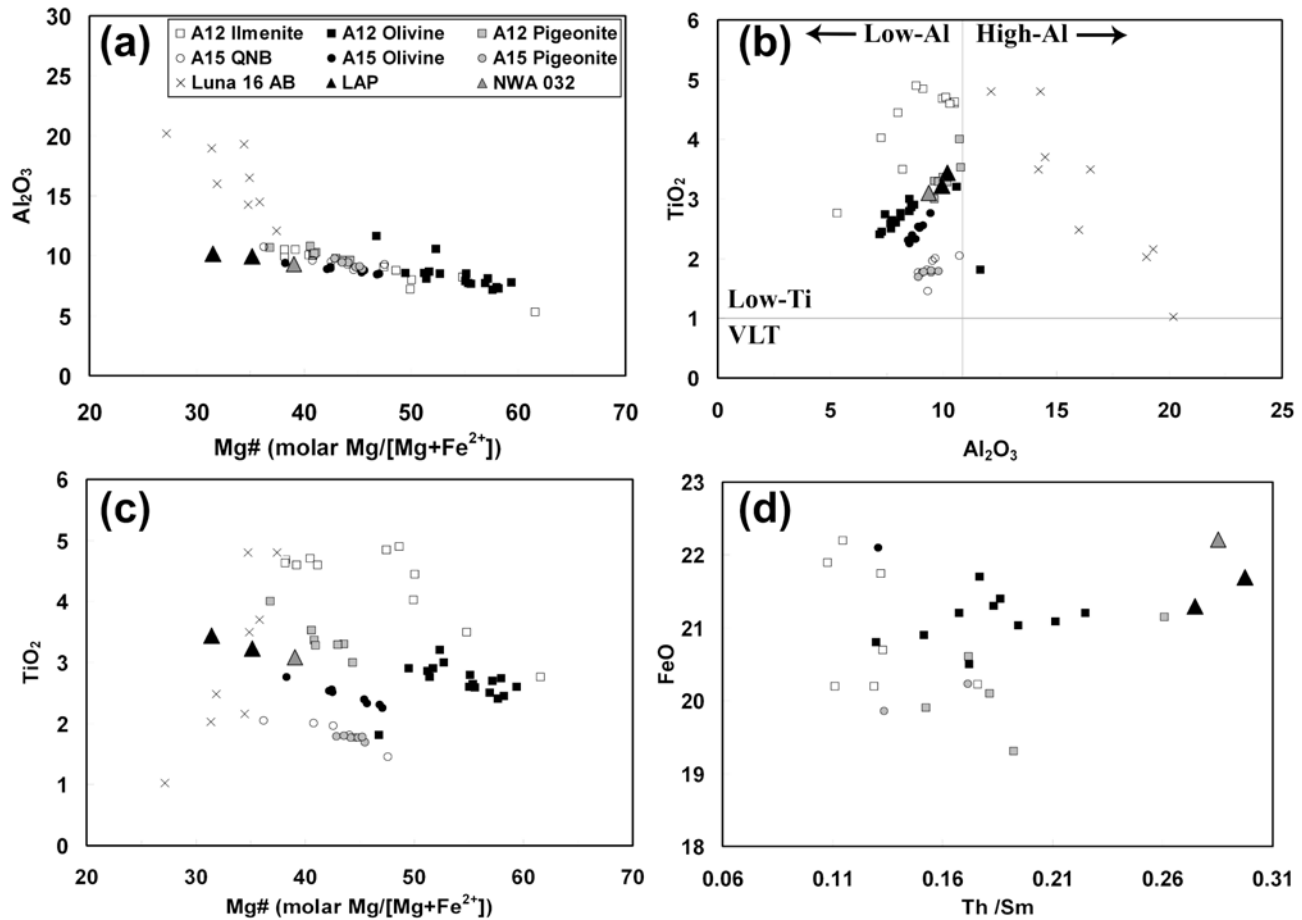
Fig. 12. Bulk composition variation diagrams comparing LAP to low-Ti basalts from the Apollo 12 (A12), Apollo 15 (A15), and Luna 16 collections. Apollo compositions are taken from Rhodes and Hubbard (1973), Rhodes et al. (1977), BVSP (1981), Neal et al. (1994a), and average bulk composition data for NWA 032 are taken from Zeigler et al. (2005). a) LAP has the lowest Mg# of the low-Al, low-Ti basalts. b) A plot of TiO_2 against Al_2O_3 shows that the LAP stones are all within the low-Ti, low-Al lunar mare basalt classification as proposed by Neal and Taylor (1992). c) TiO_2 and Mg# are good distinguishing characteristics for the Apollo basalts: the different olivine, pigeonite, ilmenite, and QNB basalts all fall into distinctive groupings, with the LAP stones not easily being fitted into any group. d) LAP, along with NWA, is highly enriched Th (and other ITEs) compared to the other basalts.

However, bulk MgO (5.58–6.47 wt%) and Mg# (35–31) is lower than typical values in these low-Ti basalts (Figs. 12a and 12b) and total bulk alkalis ($Na_2O + K_2O$) is much higher (0.51–0.54 wt%). The LAP bulk REE content is shown in Fig. 13 and is significantly higher than found in basalts collected from the Apollo 12 and Apollo 15 sites. The LAP REE values are more comparable to Apollo 14 and Luna 16 high-Al basalt rocks, though LAP has a lower bulk-Al_2O_3 content and a different magmatic origin. Elevated REE content also makes LAP distinct from the Y-793169, A-881757, and Dhofar 287a meteorites. However, Th/Sm ratios (0.297–0.275) (Fig. 12d) in LAP are similar to the proposed paired meteorite NWA 032 (Th/Sm = 0.287) (Fagan et al. 2002).

Whole rock composition for the LAP stones, as determined by ICP-OES/Mass-Spec, fused bead EMPA/ICP-MS, and INAA has recently been reported by Anand et al. (2006), Day et al. (2006), and Zeigler et al. (2005),

respectively, and is included in Table 1 for comparison. Generally, the major elements are within good agreement (to within 1 wt%), although our reported FeO is in better agreement with Day et al. (2006) than the other two techniques. Figure 14 compares the minor and trace element concentrations obtained here (Table 1) with other recently published data. It will be seen that the agreement is generally very good, although there are significant discrepancies for Ni, Cu, Zn, Ga, Cs, and W. Generally all of the REE concentrations are in good agreement (Fig. 14b), although our concentrations are 10–20% higher than those reported by Anand et al. (2006) and Zeigler et al. (2005), and 30% higher than those presented by Day et al. (2006). As our K_2O (and to a lesser extent P_2O_5) bulk composition is also elevated, particularly compared to that reported by Zeigler et al. (2005), this small enhancement in REE content may simply reflect the fact that we have analyzed samples with greater concentrations of mesostasis (and thus ITEs). Overall bulk
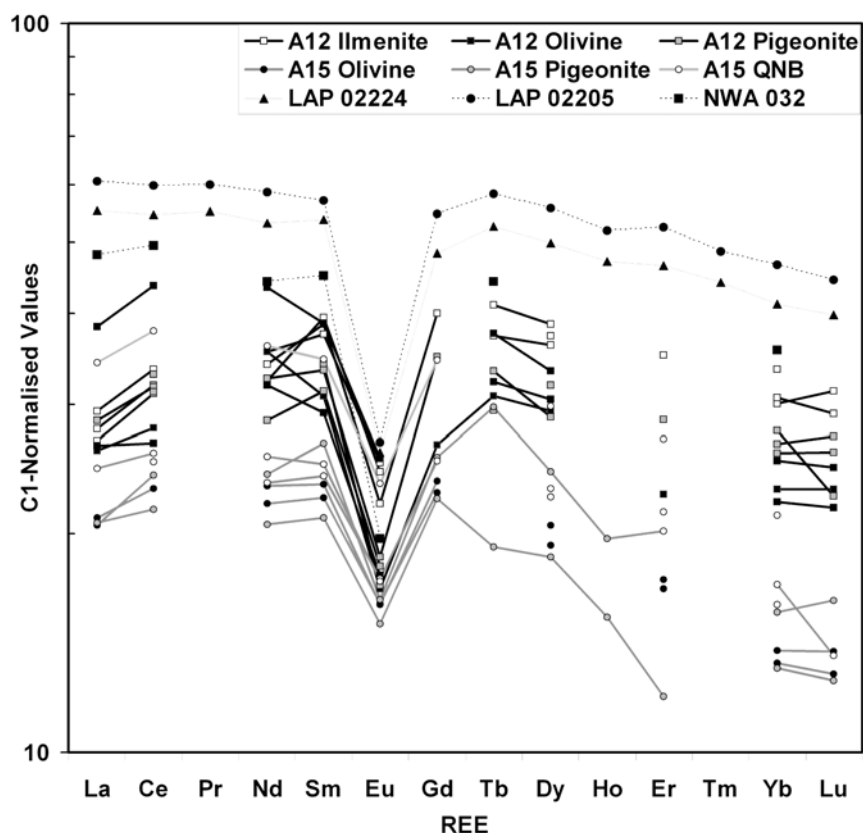
Fig. 13. Bulk rock REE concentration normalized to C1 chondrites (Anders and Grevesse 1989) for LAP 02205 and LAP 02224. Our results are compared to Apollo low-Ti suites and lunar meteorite sample NWA 032. Apollo data are taken from Rhodes and Hubbard (1973), Rhodes et al. (1977), BVSP (1981), Neal et al. (1994a); average bulk REE concentrations for NWA 032 are taken from Zeigler et al. (2005). The LAP stones are clearly the most REE enriched of the low-Ti basalts.

composition heterogeneity between the LAP 02205 and 02224 measured in this study, and between other LAP samples (e.g., Zeigler et al. 2005; Anand et al. 2006; Day et al. 2006), may be caused by short-range unmixing, where minerals settled out during fractional crystallization (causing different sections emplaced within a few cm of each other to have different concentrations of mineral phases, and therefore heterogeneous bulk compositions; e.g., Lindstrom and Haskin 1978).

Different authors have tried to align LAP directly to specific groups of samples in the Apollo collection (see Anand et al. 2006 for a summary). In terms of Mg# LAP is similar to the Luna 16 aluminous basalts and the Apollo 15 quartz-normative basalts (QNBs) (e.g., Ryder et al. 1985), but is too TiO_2 and REE-enriched to be part of this group. It is too Ti-poor and Rb/Sr-rich to be comparable with Apollo 12 ilmenite basalts, and too Mg#-poor (Figs. 12a and 12c), Co/Sm-depleted (4.12–4.85) and Sr-rich (135–143 ppm) to be part of the Apollo 12 olivine basalt suite (where Co/Sm >10 and Sr <110 ppm; Neal and Taylor 1992). Joy et al. (2005a, 2005b) proposed that the stones were most similar to the Apollo 12 pigeonite basalt suite as they have similar bulk rock Al_2O_3, MgO, TiO_2, Sr, and Co/Sm ratios. However, it is now

clear that they exhibit enriched LREE profiles, excessive Eu and Th concentrations, and lower Mg# values than most of the samples in the pigeonite suite and we now consider this earlier identification to be unlikely.

It is most probable that LAP was launched from the Moon's near side (since 30% by area of the lunar near side is basaltic, compared to only 2% of the lunar far side) (e.g., Wilhelms 1987). As it is a relatively young magmatic sample and has an elevated Th content (Table 1), it is possible that the stones were ejected from a lava flow within the PKT region, which is known to be an area of relatively young basaltic emplacement (Wilhelms 1987; Hiesinger et al. 2003). This can be more carefully constrained using remotely sensed data sets like those from the Clementine and Lunar Prospector missions, and information from new lunar missions like the Compact Imaging X-ray Spectrometer (D-CIXS) instrument (Dunkin et al. 2003) aboard ESA's SMART-1 mission.

Petrogenesis

The two samples of LAP analyzed for this study have similar bulk major element compositions (Table 1). Minor differences in MgO (~1%) are probably a consequence of the
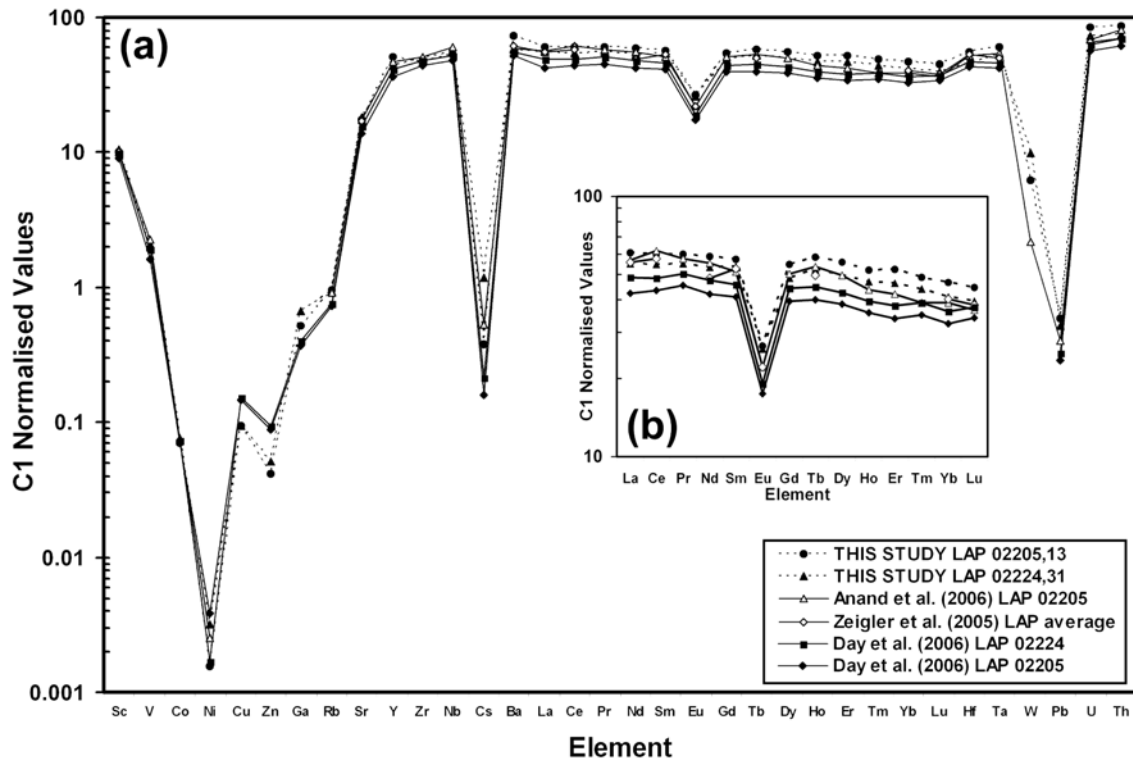
Fig. 14. The chondrite-normalized bulk rock concentrations of minor and trace elements for LAP obtained in this study compared with other recently published values. a) All minor and trace elements; b) rare earth elements (REE) only. Note that there is general agreement, but that our REE values are systematically higher, presumably reflecting the fact that our samples contain a greater concentration of mesostasis (and thus incompatible trace elements).

difference in forsteritic olivine content between the two samples (Table 5); LAP 02205 has less forsteritic olivine and therefore less MgO than 02224. Other minor compositional variations (TiO$_2$, Al$_2$O$_3$, and CaO) are a consequence of minor mineralogical heterogeneity. LAP 02205 and 02224 have very similar bulk REE patterns (Fig. 13); providing additional evidence that the rocks originate from the same lunar parent melt source. LAP 02205 shows a slight enrichment in REE, probably as a consequence of the measurement of different proportions of incompatible element enriched mesostasis regions in the two stones (Neal et al. 1994a; Day et al. 2006).

The crystallization sequence of minerals in LAP 02205 can be inferred from sample petrography, mineral elemental concentrations, and thermodynamic modeling. There is a discrepancy between petrographic inference and the results of the fractional crystallization modeling using the MELTS modeling code (Ghiorso and Sack 1995; Asimow and Ghiorso 1998). According to petrographic observation the first minerals to be crystallized was Cr-spinel that is enclosed by secondary crystallizing large forsteritic olivine grains. However, using the MELTS software with a system pressure of 1 bar and fO$_2$ set at 2.0 log units below the IW buffer (Righter et al. 2005; Day et al. 2006), our modeling predicts that the first mineral to crystallize is chromite (at 1180 °C)

followed by pyroxene (at 1137 °C) with no forsteriteic olivine phases being crystallized anywhere in the fractionation sequence. Anand et al. (2006) also report the apparent non-crystallization of Mg-rich olivine in LAP's crystallization sequence, and propose that the forsteritic olivines may be xenocrystic phases which have been incorporated into LAP from mixing in a magma chamber with the fractionated products of an earlier olivine- and Mg-rich melt. Our modeling is consistent with this interpretation and with the petrographic observation that the olivine phases often have embayed or reabsorbed rim structures, suggesting a reaction between the existing olivines and crystallizing pyroxene phases from the LAP melt.

As the melt cooled to ~1124 °C, plagioclase co-tectically crystallized with both low and high-Ca pyroxene nuclei grains (core compositions) (Figs. 5a, 5b, and 6) and spinel (increasingly Ti-rich, Cr-depleted) (Fig. 10). Fayalitic olivine grains (Mg#$_{30}$) started to co-crystallize at ~1081 °C, and as the residual liquid is depleted in Mg the crystallizing pyroxenes zone to Fe-rich species. Ilmenite arrives on the liquidus after further cooling to ~1012 °C. As compatible elements are substituted into these co-crystallizing phases the melt becomes incompatible element enriched and silica oversaturated. Late stage crystallization of silica phases occurred from about ~910–890 °C, and Fe-pigeonites,

subcalcic augites and pyroxferroite crystallized as late stage pyroxene rims. Late stage plagioclase became enriched in K and Na (Fig. 7), and spinel evolved to pure ulvöspinel compositions (Fig. 10). Residual melt pockets experienced liquid immiscibility, producing glasses emplaced in a groundmass of fayalitic olivine with associated baddelyite blebs, FeNi metal grains, and troilite. The system had almost wholly crystallized (0.34% residual liquid) by the time the lava had cooled to <851 °C.

The lunar basalt represented by the LAP meteorite is the product of fractional crystallization from a parental source melt that is similar in composition to the low-Ti source region that produced the Apollo 12 and Apollo 15 low-Ti basalts and low-Ti volcanic glasses, although it cannot be petrologically related to them due to systematic differences in ages between the Apollo and LAP basalts (Day et al. 2006). Parental melt modeling has been performed by Zeigler et al. (2005) and Righter et al. (2005), who investigated the fractional crystallization trends of a suite of potential parental melts including lunar low-Ti picritic glass and vitrophyle mare samples. Both groups of authors propose that the Apollo 15 yellow picritic glass would make a good candidate parental melt composition on the basis of major element fractionation trends (particularly CaO, TiO_2). However, Righter et al. (2005) conclude that this cannot be a parental melt for LAP on the basis of ITE modeling, as it would produce fractionates that are too high in Zr and Yb and too low in Sc. Righter et al. (2005) go on to suggest that modeling from the Apollo 12 olivine basalt suite, and in particular the olivine basalt sample 12009, produces the best candidate compositions that are similar to those of LAP (and NWA 032). However, our calculations using MELTS indicate that the Apollo 12 olivine basalts produce trends that are too TiO_2, CaO, and Al_2O_3 rich to truly match with the LAP (and NWA 032) fractionation trend. Moreover, Neal et al. (1994a, 1994b) showed that, at the Apollo 12 site, the ilmenite, olivine, and pigeonite suites are representative of three separate parent magmatic bodies and are independently derived from distinct source regions. This heterogeneity at just one Apollo landing site is indicative of the complexity of mare basalt magmatic generation, and at present the LAP parental source cannot be accurately characterized from available samples in the Apollo collection. We therefore conclude that the LAP stones represent evolved types of low-Ti, low-Al, and low-K basalts that are unique samples of young mare basalt material.

LAP has elevated REE abundances compared to other low-Ti basaltic samples (although it has long been recognized that high-Ti basalts from the Apollo 11 and 17 landing sites, the Luna 16 high-Al basalts, and KREEP basalts exhibit comparable, or higher, REE enrichments; e.g., Beatty et al. 1979, Papike et al. 1998). The elevated REE abundances in LAP in comparison to other low-Ti basalts (Fig. 13) resemble those in the comparably "young" (2.78 Ga [Fernandes et al. 2003]; 2.87 Ga [Borg et al. 2004]) lunar olivine cumulate NWA 773 (Jolliff et al. 2003; Day et al. 2006). Indeed,

comparison of Fig. 13 with Fig. 7 of Jolliff et al. (2003) shows LAP to be even more REE enhanced. It has been argued by Jolliff et al. (2003) and Borg et al. (2004) that the elevated REE concentrations in NWA 773 are indicative of a KREEP-rich component in the source region, the heat-producing elements in which may have been responsible for maintaining magmatic activity until a relatively late date. In principle, a similar argument could be constructed for LAP and NWA 032, but only if it can be shown that the enhanced REE abundances cannot be obtained by normal fractionation processes. Day et al. (2006) have investigated the possibility that LAP formed as a result of assimilation fractional crystallization (AFC) processes, whereby mantle-derived KREEP material was included into the melt to account for the high REE abundances. However, they concluded that this hypothesis is difficult to reconcile with the REE systematics in pyroxenes, which exhibit a normal fractionation trend—suggesting a closed system and that any ITE assimilation must have occurred prior to the onset of pyroxene crystallization. Clearly, additional samples of young basaltic materials are required to determine whether or not there exists a general trend of increasing ITE concentration with decreasing age, as might be expected if a KREEP component is required to drive late magmatic activity.

SUMMARY

The LAP stones are important additions to the lunar rock collection. The three samples studied in this paper have a very similar bulk composition and mineralogy, and the small differences among them are likely to result from short-range unmixing. Thus, they appear to be derived from a single, relatively young (~2.9 Ga; Anand et al. 2006), lava flow on the lunar surface. The presence of a vesicular fusion crust on LAP 02224, the first identified in any lunar crystalline basaltic sample, implies that it was at one time located sufficiently close to the lunar surface to have accumulated solar wind implanted gases.

We concur with Zeigler et al. (2005), Righter et al. (2005), Anand et al. (2006), and Day et al. (2006) that the bulk rock compositions of the LAP stones are most similar to the Apollo 12 low-Ti, low-Al basalt group. However, they cannot be directly classed with any site-specific lithology as they are significantly enriched in REE, have systematically different major element compositions, and lower Mg# numbers than characterize Apollo and Luna basalt samples. Rather, LAP is interpreted to be a product of fractional crystallization from a Fe-rich source, which experienced extreme fractionation with late-stage liquid immiscibility and REE enrichment in pockets of mesostasis. Thermodynamic modeling by ourselves (see above) and others (e.g., Righter et al. 2005; Zeigler et al. 2005; Day et al. 2006) has been used to try to constrain a potential parental melt composition, but as of yet there is no identified source composition that could produce fractionates with bulk compositions that match the

LAP basalt. Thus, the LAP stones appear to represent part of a previously unsampled, young, low-Al, low-Ti mare basalt suite, possibly from within the PKT. Future work is intended to address the provenance of these basaltic meteorites by using geochemical information from orbital remote-sensing instruments, combined with relative age indicators from crater counting techniques.

Editorial Handling—Dr. Randy Korotev

REFERENCES

Anand M., Taylor L. A., Neal C. R., Snyder G. A., Patchen A., Sano Y., and Terada K. 2003a. Petrogenesis of lunar meteorite EET 96008. *Geochimica et Cosmochimica Acta* 67:3499–3518.

Anand M., Taylor L. A., Misra K. C., Deminova S. I., and Nazarovi M. A. 2003b. KREEPy lunar meteorite Dhofar 287a: A new lunar mare basalt. *Meteoritics & Planetary Science* 38:485–499.

Anand M., Taylor L. A., Floss C., Neal C., Terada K., and Tanikawa S. 2006. Petrology and geochemistry of LaPaz Icefield 02205: A new unique low-Ti mare-basalt meteorite. *Geochimica et Cosmochimica Acta* 70:246–264.

Anders E. and Grevesse N. 1989. Abundances of the elements: Meteoritic and solar. *Geochimica et Cosmochimica Acta* 53:97–214.

Arai T., Takeda H., and Warren P. H. 1996. Four lunar mare meteorites: Crystallization trends of pyroxenes and spinels. *Meteoritics & Planetary Science* 33:877–892.

Arai T., Ishi T., and Otsuki M. 2002. Mineralogical study of new lunar meteorite Yamato 981031 (abstract #2064). 33rd Lunar and Planetary Science Conference. CD-ROM.

Aramovich C. J., Head C. D. K., and Papike J. J. 2001. Possible causes for late-stage reaction textures associated with pyroxferroite and metastable pyroxenes in the basaltic Martian meteorites (abstract #1003). 32nd Lunar and Planetary Science Conference. CD-ROM.

Asimow P. D. and Ghiorso M. S. 1998. Algorithmic modifications extending MELTS to calculate subsolidus phase relations. *American Mineralogist* 83:1127–1131.

Basaltic Volcanism Study Project. 1981. Lunar mare basalts. In *Basaltic volcanism on the terrestrial planets*. New York: Pergamon Press. pp. 236–266.

Beatty D. W., Hill S. M. R., Albee A. L., Ma M.-S., and Schmitt R. A. 1979. The petrology and chemistry of basaltic fragments from the Apollo 11 soil, part I. Proceedings of the 10th Lunar and Planetary Science Conference. pp. 41–75.

Bischoff A., Weber D., Clayton R. N., Faestermann T., Franchi I. A., Herpers U., Knie K., Korschinek G., Kubik P. W., Mayeda T. K., Merchel S., Michel R., Neumann S., Palme H., Pillinger C. T., Schultz L., Sexton A. S., Spettel B., Verchovsky A. B., Weber

H. W., Weckwerth G., and Wolf D. 1998. Petrology, chemistry, and isotopic compositions of the lunar highland regolith breccia Dar al Gani 262. *Meteoritics & Planetary Science* 33:1243–1257.

Borg L. E., Shearer C. K., Asmerom Y., and Papike J. J. 2004. Prolonged KREEP magmatism on the Moon indicated by the youngest dated lunar igneous rock. *Nature* 432:209–211.

Cahill J. T., Floss C., Anand M., Taylor L. A., Nazarov M. A., and Cohen B. A. 2004. Petrogenesis of lunar highlands meteorites: Dhofar 025, Dhofar 081, Dar al Gani 262, and Dar al Gani 400. *Meteoritics & Planetary Science* 39:503–530.

Day J. M. D., Pearson D. G., and Taylor L. A. 2005. ^{187}Re-^{187}Os isotope disturbance in LaPaz mare basalt meteorites (abstract #1424). 36th Lunar and Planetary Science Conference. CD-ROM.

Day J. M. D., Taylor L. A., Floss C., Patchen A. D., Schnare D. W., and Pearson D. G. 2006. Comparative petrology, geochemistry and petrogenesis of evolved, low-Ti lunar mare basalt meteorites from the LaPaz icefield, Antarctica. *Geochimica et Cosmochimica Acta* 70:1581 –1600.

Dymek R. F., Albee A. L., Chodos A. A., and Wasserburg G. J. 1976. Petrography of isotopically-dated clasts in the Kapoeta howardite and petrologic constraints on the evolution of its parent body *Geochimica et Cosmochimica Acta* 40:1115–1116.

Dunkin S. K., Grande M., Casanova I., Fernandes V., Heather D. J., Kellett B., Muinonen K., Russell S. S., Browning R., Waltham N., Parker D., Kent B., Perry C. H., Swinyard B., Perry A., Feraday J., Howe C., Phillips K., McBride G., Huovelin J., Muhli P., Hakala P. J, Vilhu O., Thomas N., Hughes D., Alleyne H., Grady M., Lundin R., Barabash S., Baker D., Clark P. E., Murray C. D., Guest J., d'Uston L. C., Maurice S., Foing B., Christou A., Owen C., Charles P., Laukkanen J., Koskinen H., Kato M., Sipila K., Nenonen S., Holmstrom M., Bhandari N., Elphic R., and Lawrence D. 2003. Scientific rationale for the D-CIXS X-ray spectrometer on board ESA's SMART-1 mission to the Moon. *Planetary and Space Science* 51:435–442.

El Goresy A., Prinz M., and Ramdohr P. 1976. Zoning in spinels as an indicator of the crystallization histories of mare basalts. Proceedings, 7th Lunar Science Conference. pp. 1261–1279.

Fagan T. J., Taylor G. J., Keil K., Bunch T. E., Wittke J. H., Korotev R. L., Jolliff B. L., Gillis J. J., Haskin L. A., Jarosewich E., Clayton R. N., Mayeda T. K., Fernandes V. A., Burgess R., Turner G., Eugster O., and Lorenzetti S. 2002. Northwest Africa 032: Product of lunar volcanism. *Meteoritics & Planetary Science* 37:371–394.

Fernandes V. A., Burgess R., and Turner G. 2003. ^{40}Ar-^{39}Ar chronology of lunar meteorites NWA 032 and 773. *Meteoritics & Planetary Science* 38:555–564.

Ghiorso M. S. and Sack R. O. 1995. Chemical mass transfer in magmatic processes. IV. A revised and internally consistent thermodynamic model for the interpolation and extrapolation of liquid-solid equilibria in magmatic systems at elevated temperatures and pressures. *Contributions to Mineralogy and Petrology* 119:197–212.

Hiesinger H. H., Head J. W. III, Wolf U., Jaumann R., and Neukum G. 2003. Ages and stratigraphy of mare basalts in Oceanus Procellarum, Mare Nubium, Mare Cognitum, and Mare Insularum. *Journal of Geophysical Research* 108:5065.

Jolliff B. L., Gillis J. J., Haskin L. A., Korotev R. L., and Wieczorek M. A. 2000. Major lunar crustal terranes: Surface expressions and crust-mantle origins. *Journal of Geophysical Research* 105:4197–4216.

Jolliff B. L., Korotev R. L., Zeigler R. A., and Floss C. 2003. Northwest Africa 773: Lunar mare breccia with a shallow-formed olivine-cumulate component, inferred very-low-Ti

(VLT) heritage, and a KREEP connection. *Geochimica et Cosmochimica Acta* 67:4857–4879.

Joy K. H., Crawford I. A., Russell S. S., and Kearsley A. T. 2005a. LAP 02205, LAP 02224, and LAP 02226—Lunar Mare Basaltic Meteorites. Part 1: Petrography and mineral chemistry (abstract #1697). 36th Lunar and Planetary Science Conference. CD-ROM.

Joy K. H., Crawford I. A., Russell S. S., and Kearsley A. T. 2005b. LAP 02205, LAP 02224 and LAP 02226—Lunar mare basaltic meteorites. Part 2: Geochemistry and crystallization (abstract #1701). 36th Lunar and Planetary Science Conference. CD-ROM.

Koizumi E., Chokai J., Mikouchi M., Makishima J., and Miyamoto M. 2005. Crystallization of lunar mare meteorite LAP 02205 (abstract #5152). 68th Meeting of the Meteoritical Society. CD-ROM.

Korotev R. L. 1991. Apollo 16 impact melt breccias 1: Intrasample compositional variations and their causes (abstract). 22nd Lunar and Planetary Science Conference. p. 743.

Korotev R. L. 2005. Lunar geochemistry as told by lunar meteorites. *Chemie der Erde* 65:297–346.

Lindstrom M. M. and Haskin L. A. 1978. Caused of compositional variations within mare basalt suites. Proceedings, 9th Lunar and Planetary Science Conference. p. 465–486.

Neal C. R. and Taylor L. A. 1989. Metasomatic products of the lunar magma ocean: The role of KREEP dissemination. *Geochimica et Cosmochimica Acta* 53:529–541.

Neal C. R. and Taylor L. A. 1992. Petrogenesis of mare basalts: A record of lunar volcanism. *Geochimica et Cosmochimica Acta* 56:2177–2211.

Neal C. R., Hacker M. D., Snyder G. A., Taylor L. A., Lui Y.-G., and Schmitt R. A. 1994a. Basalt generation at the Apollo 12 site, part 1: New data, classification, and re-evaluation. *Meteoritics* 29:334–348.

Neal C. R., Hacker M. D., Snyder G. A., Taylor L. A., Lui Y.-G., and Schmitt R. A. 1994b. Basalt generation at the Apollo 12 site, part 2: Source heterogeneity, multiple melts, and crustal contamination. *Meteoritics* 29:349–361.

Nielsen R. J. and Drake M. J. 1978. The case for at least three mare basalt magmas at the Luna 24 site. In *Mare Crisium: The view from Luna 24*, edited by Merrill R. B. and Papike J. J. New York: Pergamon. pp. 419–428.

Nishiizumi K., Hillegonds D. J., and Welten K. C. 2006. Exposure and terrestrial histories of lunar meteorites LAP 02205/02224/02226/02436, MET 01210, and PCA 02007 (abstract #2369). 37th Lunar and Planetary Science Conference.

Nyquist L. E., Shih C.-Y., Reese Y., and Bogard D. D. 2005. Age of lunar meteorite LAP 02205 and implications for impact-sampling of planetary surfaces (abstract #1374). 36th Lunar and Planetary Science Conference. CD-ROM.

Papike J. J., Taylor L., and Simon S. 1991. Lunar minerals. In *Lunar sourcebook: A user's guide to the Moon*, edited by Heiken G. H., Vaniman D., and French B. M. Cambridge: Cambridge University Press. 736 p.

Papike J. J. 1998. Comparative planetary mineralogy: Chemistry of melt-derived pyroxene, feldspar, and olivine. In *Planetary materials*, edited by Papike J. J. Washington, D.C.: Mineralogical Society of America. pp. 7-1–7-11.

Papike J. J., Ryder G., and Shearer C. K. 1998. Lunar samples. In *Planetary materials*, edited by Papike J. J. Washington, D.C.: Mineralogical Society of America. pp. 5-1–5-234.

Papike J. J., Karner J. M., and Shearer C. K. 2003. Determination of planetary basalt parentage: A simple technique using the electron microprobe. *American Mineralogist* 88:469–472.

Rankenburg K., Brandon A., Norman M., and Righter K. 2005. LAP 02 205: An evolved member of the Apollo 12 olivine basalt suite? (abstract) *Meteoritics & Planetary Science* 40:A125.

Rhodes J. M. and Hubbard N. J. 1973. Chemistry, classification, and petrogenesis of Apollo 15 mare basalts. Proceedings, 4th Lunar Science Conference. pp. 1127–1148.

Rhodes J. M., Brannon J. C., Rodgers K. V., Blanchard D. P., and Dungan M. A. 1977. Chemistry of Apollo 12 mare basalts—Magma types and fractionation processes. Proceedings, 8th Lunar Science Conference. pp. 1305–1338.

Righter K., Brandon A. D., and Norman M. D. 2004. Mineralogy and petrology of unbrecciated lunar basaltic meteorite LAP 02205 (abstract #1667). 35th Lunar and Planetary Science Conference. CD-ROM.

Righter K., Collins S. J., and Brandon A. D. 2005. Mineralogy and petrology of the LaPaz Icefield lunar mare basaltic meteorites. *Meteoritics & Planetary Science* 40:1703–1722.

Roedder E. and Weiblen P. W. 1977. Compositional variation in late-stage differentiates in mare lavas, as indicated by silicate melt inclusions. Proceedings, 8th Lunar Science Conference. pp. 1767–1783.

Rubin A. E., Scott E. R. D., and Keil K. 1997. Shock metamorphism of enstatite chondrites. *Geochimica et Cosmochimica Acta* 61: 847–858.

Ryder G. 1985. *Catalog of Apollo 15 rocks*. Houston, Texas: NASA Johnson Space Center. 1296 p.

Satterwhite C. E., editor. 2003. *Antarctic Meteorite Newsletter* 26(2).

Satterwhite C. E., editor. 2004a. *Antarctic Meteorite Newsletter* 27(1).

Satterwhite C. E., editor. 2004b. *Antarctic Meteorite Newsletter* 27(3).

Stöffler D., Keil K., and Scott E. R. D. 1991. Shock metamorphism of ordinary chondrites. *Geochimica et Cosmochimica Acta* 55: 3845–3867.

Synder G. A., Taylor L. A., and Halliday A. N. 1995. Chronology and petrogenesis of the lunar highlands suite: Cumulates from KREEP basalt crystallization *Geochimica et Cosmochimica Acta* 59:1185–1203.

Taylor L. A. and Misra K. C. 1975. Pyroxene-phyric basalt 15075: Petrography and petrogenesis. Proceedings, 6th Lunar Science Conference. pp. 165–179.

Taylor L. A and Day J. M. D. 2005. FeNi metal grains in LaPaz mare basalt meteorites and Apollo 12 basalts (abstract #1417). 36th Lunar and Planetary Science Conference. CD-ROM.

Thompson M. and Walsh J. N. 2003. *Handbook of inductively coupled plasma atomic emission spectrometry*. Woking, Surrey: Viridian Publishing.

Warren P. H. 2005. "New" lunar meteorites: Implications for composition of the global lunar surface, lunar crust, and the bulk Moon. *Meteoritics & Planetary Science* 40:477–506.

Weiblen P. W. Examination of the liquid line of descent of mare basalts in light of data from melt inclusions in olivine. 1977. Proceedings, 8th Lunar Science Conference. pp. 1751–1765.

Wilhelms D. E. 1987. General features. In *The geologic history of the Moon*. US Geological Survey Professional Paper 1348.

Vaniman D., Dietrich J., Taylor G. J., and Heiken G. Exploration, samples, and recent concepts of the Moon. 1991. In *Lunar sourcebook: A user's guide to the Moon*, edited by Heiken G. H., Vaniman D., and French B. M. Cambridge: Cambridge University Press.

Zeigler R. A., Korotev R. L., Jolliff B. L., and Haskin L. A. 2005. Petrology and geochemistry of the LaPaz icefield basaltic lunar meteorite and source-crater pairing with Northwest Africa 032. *Meteoritics & Planetary Science* 40:1073–1102.